ADVANCED FUNCTIONAL MATERIALS
www.afm-journal.de

Detection and Signal Processing for Near-Field Nanoscale Fourier Transform Infrared Spectroscopy

Jonathan M. Larson, Hans A. Bechtel,* and Robert Kostecki**

Researchers from a broad spectrum of scientific and engineering disciplines are increasingly using scattering-type near-field infrared spectroscopic techniques to characterize materials non-destructively with nanoscale spatial resolution. However, a sub-optimal understanding of a technique's implementation can complicate data interpretation and act as a barrier to entering the field. Here the key detection and processing steps involved in producing scattering-type near-field nanoscale Fourier transform infrared spectra (nano-FTIR) are outlined. The self-contained mathematical and experimental work derives and explains: i) how normalized complex-valued nano-FTIR spectra are generated, ii) why the real and imaginary components of spectra qualitatively relate to dispersion and absorption respectively, iii) a new and generally valid equation for spectra which can be used as a springboard for additional modeling of the scattering processes, and iv) an algebraic expression that can be used to extract an approximation to the sample's local extinction coefficient from nano-FTIR. The algebraic model for weak oscillators is validated with nano-FTIR and attenuated total reflectance Fourier transform infrared (ATR-FTIR) spectra on samples of polystyrene and Kapton and further provides a pedagogical pathway to cementing some of the technique's key qualitative attributes.

1. Introduction

For at least half a century, Fourier transform infrared spectroscopy (FTIR) has been regarded as a gold standard for nondestructive chemical and structural fingerprinting.[1] This is due to the relatively low energy of infrared (IR) light, and the technique's sensitivity to changing electric dipole moments, such as those in molecular and crystal lattice vibrations. Moreover, the vast majority of materials are IR active and possess a unique IR spectrum signature, thus FTIR is ubiquitous in both academia and industry. Unfortunately, because of the relatively long wavelengths of infrared light and related diffraction limit, the spatial resolution for FTIR has been limited to ≈ 1–1000 μm.[2] Thus, FTIR's utilization during the so-called "nano-revolution"[3] during the last ≈ 35 years has played an insignificant role in the characterization of nanostructures and associated nanoscale phenomena due to its inadequate spatial resolution. However, over the last decade, with the coalescence of scattering-type, scanning near-field optical microscopy (s-SNOM),[4] high-power broadband IR sources, IR interferometry, and lock-in amplification techniques, scattering-type near-field nanoscale Fourier transform IR spectroscopy (nano-FTIR) has been realized,[5] commercialized, and its utilization has grown significantly in recent years.

The broad appeal and impact of nano-FTIR as a tool for sensing local IR-active physicochemical phenomena has been demonstrated by a large number of studies that span the gamut of science, technology, and engineering. A non-exhaustive subset of the many and diverse focus topics are nanoconfinement in metal–organic frameworks,[6] probing interphases between hard and soft condensed matter,[7] mapping catalytic reactions,[8] antenna assisted characterization of dielectric anisotropy,[9] phonon polaritons,[10] insulator–metal transitions,[11] mapping strain in 2D materials,[12] nanoscale dielectric properties,[13] organic matter contents of meteorites,[14] spectroscopic nanoimaging,[15] nonequilibrium physics,[16] battery electrode materials,[17] electrochemical interfaces and interphases,[17b,18] twisted moire superlattices,[19] nonequilibrium polariton switching and control at ultrafast timescales,[20] and biological studies of biomineralization,[21] proteins,[22] viruses,[23] linkers for biomolecule targeting,[24] living cells,[25] and spike proteins on COVID-19 viruses.[26] Additionally, motivated by the technique's clear success, new developments, implementations, simulations, and models, are continuing to emerge, such as ultrafast heterodyne pump-probe,[27] Purcell-enhanced IR approaches,[28] simulating hyperspectral images of 3D

J. M. Larson
Department of Chemistry and Biochemistry
Baylor University
Waco, TX 76798, USA
E-mail: jonathan_larson@baylor.edu
J. M. Larson, R. Kostecki
Energy Storage & Distributed Resources Division
Lawrence Berkeley National Laboratory
Berkeley, CA 94720, USA
E-mail: r_kostecki@lbl.gov
H. A. Bechtel
Advanced Light Source
Lawrence Berkeley National Laboratory
Berkeley, CA 94720, USA
E-mail: habechtel@lbl.gov
The ORCID identification number(s) for the author(s) of this article can be found under https://doi.org/10.1002/adfm.202406643

DOI: 10.1002/adfm.202406643

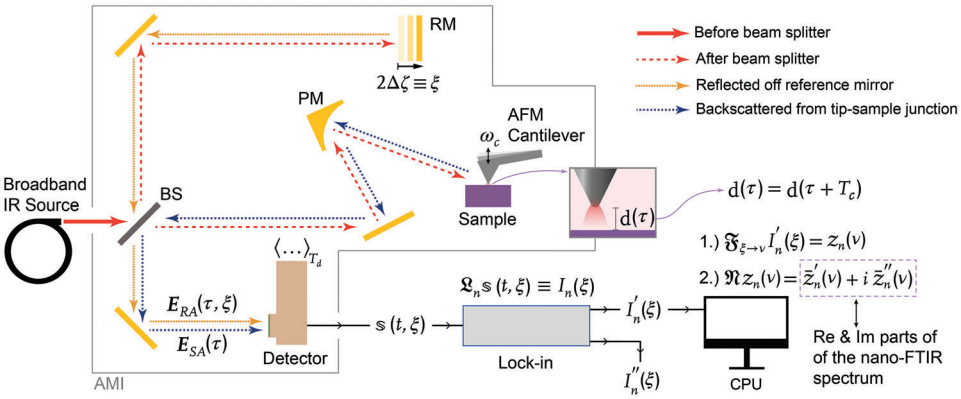

Figure 1. Schematic of the experimental setup and processing steps for scattering scanning near-field nanoscale Fourier transform infrared spectroscopy. The operator notation that is used in the rest of the text matches the diagram: detector time averaging ($\langle \ldots \rangle_{T_d}$), lock-in amplification ($\mathfrak{L}$), Fourier transformation ($\mathfrak{F}$), and normalization ($\mathfrak{N}$).

heterogeneous surfaces,[29] and modeling near-field microscopy and spectroscopy.[30]

Unfortunately, the detection scheme that underpins and enables the experimental realization of nano-FTIR is nontrivial. This methodological complexity, coupled with the diversity in practitioner-field expertise, creates an environment ripe for theoretical and conceptual barriers to robust understanding of i) the detection and signal processing steps that generate and explain the complex-valued nano-FTIR spectrum, and ii) the electrodynamic scattering process that takes place within the tip-sample region. There have been a number of publications treating the latter,[13a,30c,31] but a need persists for a rigorous and self-contained work that addresses the former — this is the aim of the present work.

We note that several photothermal approaches for IR imaging and nano-spectroscopy have also been recently pioneered[32] (e.g., nanoIR, AFM-IR, PTIR, PFIR, and PiFM). These techniques are distinct in their implementation and working mechanisms from nano-FTIR. Instead of collecting and analyzing backscattered light (as is the case for nano-FTIR) these approaches typically sense changes in AFM probe properties that can be attributed to thermal expansions or forces associated with local IR absorption and have been reviewed elsewhere.[32c,33] These are not the subject of this work.

2. Results and Discussion

2.1. Experimental Setup and Data Acquisition Summary

To provide a qualitative explanation for each of the essential steps involved with nano-FTIR acquisition, and identify key experimental components along the way; **Figure 1** serves as a critical visual aid and reference throughout the paper. First, a metal-coated atomic force microscope (AFM) probe oscillating at $\approx 10^2$ kHz (period $T_c = 10$ µs and tip-sample distance $d(\tau)$) is brought into tapping mode[34] with a substrate of interest (Figure 1) and positioned above a location of interest. Broadband IR light is introduced (solid red arrow on the left-hand side of Figure 1) into a portion of the experimental setup whose combined constituents function as an asymmetric Michelson interferometer[5f,35] (AMI, items within the gray box in Figure 1). The asymmetric terminology speaks to the difference with respect to symmetric interferometers, which are typically used in conventional FTIR. Symmetric interferometers situate the sample of interest after the interferometer, while in asymmetric setups the sample is placed within, and is part of, the interferometer itself. As will be shown in detail later, a key advantage to the asymmetric setup is that the mathematical (Fourier) transformation of data collected yields both optical amplitude and phase (or real and imaginary) information that is used to quantify sample properties.

The broadband IR light source is typically produced via difference frequency generation (DFG) with a fiber–laser[5c] (broadband) or a synchrotron[5d,h,i] (ultrabroadband), although other sources such as high-temperature plasmas are also available.[36] The typical detectable bandwidths of these two sources are shown in **Figure 2**. As a quick aside, we note that when the light source is a broadband IR laser, nano-FTIR is the commonly used acronym. However, when the light source is an ultrabroadband synchrotron, SINS (synchrotron infrared nanospectroscopy) is the commonly used acronym. In both cases, however, the signal

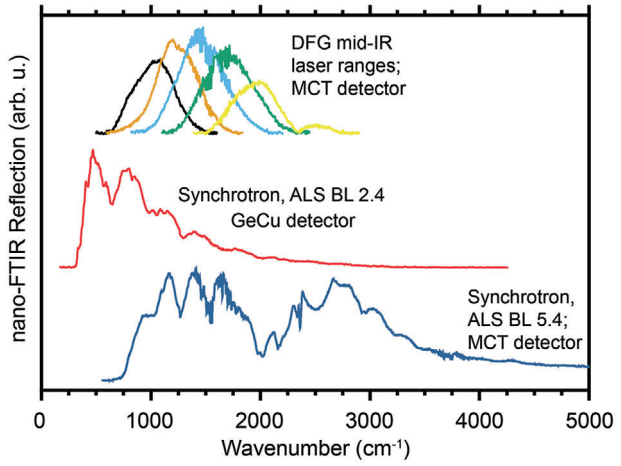

Figure 2. Raw, unnormalized, nano-FTIR reflection spectra of Au or Si for selected broadband infrared light sources.

processing and detection scheme is the same. Herein, we use the nano-FTIR acronym as encompassing both these approaches. We also note, while not the subject of this paper, that IR nanoscale spectroscopy can also be technically accomplished with a single frequency light source that is tunable, via pseudoheterodyne detection.[4a]

As the broadband light enters the AMI (solid red arrow on the left-hand side of Figure 1), it first passes through a beam splitter (BS in Figure 1). As the name implies, the BS splits the beam in two, sending each half in a different direction (see red dashed arrows in Figure 1). Half the beam is reflected, and travels toward a reference mirror (RM, top middle Figure 1), while the other half is transmitted and travels toward the AFM tip-sample region. These unique beam paths are referred to as the "reference arm" and "sample arm" of the AMI, respectively. Both arms return light (dotted yellow and blue arrows in Figure 1), which is recombined and measured at the detector (bottom right of AMI in Figure 1).

Within the reference arm, as illustrated in Figure 1, the light travels to (red dashed arrows) and reflects off (yellow dotted arrows) the RM, then transmits through the BS, before combining with light from the sample arm and being detected. It is important to make clear that the RM is movable. In particular, during nano-FTIR data acquisition, the RM will linearly translate, changing the path length difference between the sample and reference arms. During this translation, the sample and reference arm path lengths should be approximately similar, and exactly similar for a brief part of the scan; a position known as the zero path difference, or ZPD. Herein, we assign a generalized coordinate, ζ, to identify the spatial position of the RM. Any change in the RM position by some $\Delta\zeta$ (as shown in Figure 1) will change the distance the reference light will need to travel in the reference arm before detection. Specifically, the change in reference beam travel distance before detection will be $2\Delta\zeta$, where the factor of two arises from light traveling both to, and from, the RM. Thus, translating the RM amounts to shifting the reference beam in space by an amount $2\Delta\zeta$, say ξ, and therefore the total signal detected will be a function of ξ.

The light entering the sample arm of the AMI is focused with a parabolic mirror (PM in Figure 1) toward the tip-sample region. A fraction of this incident light is backscattered along the same beam path from where it came (see blue dotted arrows in Figure 1). Eventually, it recombines with the reference light and is subsequently detected. The light backscattered from the region around the sample and vertically oscillating (**Figure 3a**) metallic AFM probe can be considered a linear combination of two distinct fields, classified by the "kind" of light that drives the scattering. The first kind, and most intuitive, is the conventional diffraction-limited incident IR that bathes the entire tip-sample region in "far-field" light (red arrows and shading in Figure 3d,e). The second kind is the diffraction-limit-breaking "near-field" — induced by the incident IR in combination with probe conductivity and geometry — which is both enhanced and spatially confined in comparison to the incident IR[13a,30c,31e,h,i] (darker red shading in Figure 3f,g). The former drives "far-field scattering" from the sample and AFM probe shank (Figure 3d,e) which dominates the total backscattered signal, while the latter drives "near-field scattering" from a nanoscopic volume around the probe tip end (Figure 3f,g). Because of this, as will be discussed in more detail later, the relevant electric field component of light backscattered from the tip-sample region will be described as a linear combination of these two contributors: $E_{SA} = E^{FF} + E^{NF}$, where *SA*, *FF*, and *NF* refer to sample arm, far-field, and near-field, respectively. We note here that the specific details of probe shape, size, and composition play a crucial role in how the scattering occurs and others have made important progress in identifying ideal probe tips.[37] Our work, as will be seen later, derives general expressions that can accommodate any probe geometry and composition.

As the AFM cantilever oscillates, far-field scattering from the sample and probe shank, E^{FF}, is only modestly altered (Figure 3b,d,e), while near-field scattering, E^{NF}, dramatically changes with the tip-sample separation distance (Figure 3c,f,g). In particular, the enhanced near-field strongly interacts with the sample at the points in time of least tip-sample distance (Figure 3a,c,f,g)), causing photons to be periodically scattered from the local region at and under the probe tip's end. This small portion of the total backscattered light is attributable to scattering processes occurring within nanoscopic volumes around the probe tip end and carries local materials properties encoded within it. Therefore, the entire aim/goal of the detection and signal processing scheme is to extract this localized information.

In the following section, we present physics-based continuum mathematical models for the detection and signal processing steps, which ultimately extract meaningful information from the signal sensed by the detector, as a function of time and reference mirror position. We first provide the order-of-magnitude timescales at play (the periods) in the experimental system: IR field oscillations ($T_{IR} = 10^{-14}$ s), detector time resolution ($T_d = 10^{-6}$ s), cantilever oscillation ($T_c = 10^{-5}$ s), and the lock-in time averaging period ($T_L = 10^{-4}$ s). Second, we mention how variable independence between t and ξ is practically attained. There are two ways that ensure such independence: collecting time-dependent data at a fixed mirror position, or by moving the mirror significantly slower than any other relevant timescale. Regardless of how this is technically implemented, t and ξ are treated as independent variables in this work.

2.2. Detector Time-Averaging $\langle \ldots \rangle_{T_d}$ and Mathematical Framework

The infrared detector, usually a liquid nitrogen-cooled mercury cadmium telluride (MCT) (or another, e.g., a liquid helium cooled copper doped germanium (GeCu) detector[5h]), measures irradiance (the time-averaged electromagnetic energy per area per time) over some photodetector area a. More specifically, it measures time-averaged electromagnetic energy transferred from the Poynting vector, $\boldsymbol{S}$, (**Figure 4**). The time-averaging period is dictated by hardware, and as mentioned above, is typically $T_d = 10^{-6}\ s = 1\ \mu s$. Thus, the magnitude of the detector signal depends on a time average, over T_d, of the Poynting vector at the detector surface: $\mathbb{s}(t,\xi) = \langle \eta \int \boldsymbol{S}(\boldsymbol{x}_d, \tau, \xi) \cdot \hat{\boldsymbol{x}} da \rangle_{T_d}$. Here, $\mathbb{s}(t,\xi)$ is the real-valued signal output from the detector, η is some constant for energy conversion between the field energy and the photodetector (at $x = 0$), $\boldsymbol{S}(\boldsymbol{x}_d, \tau, \xi)$ is the Poynting vector at the detector surface, $\hat{\boldsymbol{x}}$ is the unit vector inward and normal to the detector surface, the brackets $\langle \cdots \rangle_{T_d}$ indicate a time-average over T_d, the

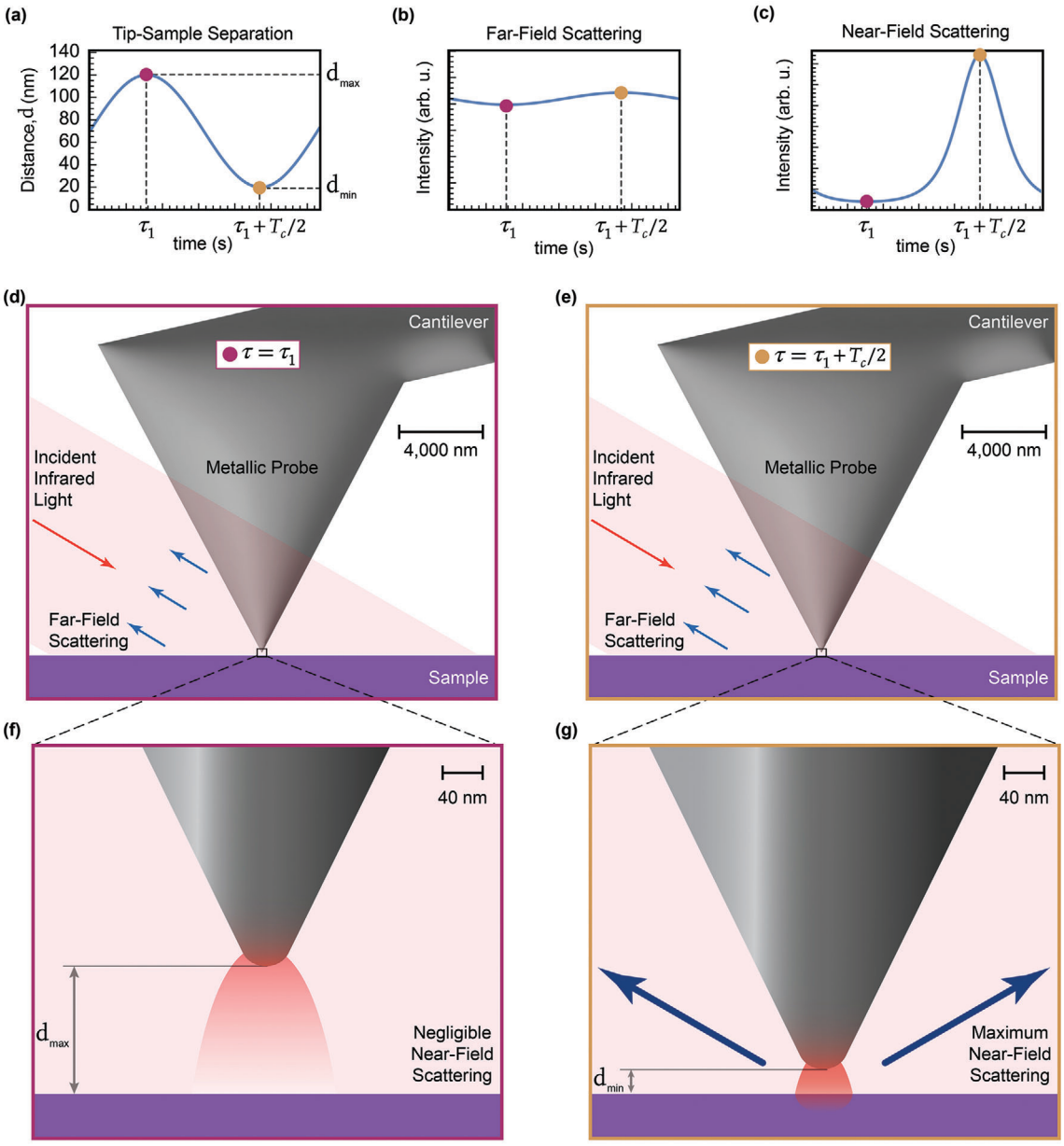

Figure 3. Representative semi-quantitative plots of the typical a) tip-sample separation distance,[30c] b) far-field scattering intensity, and c) near-field scattering intensity as a function of time, over one cantilever period, T_c. Key points in time associated with the greatest ($\tau = \tau_1$) and least ($\tau = \tau_1 + T_c/2$) tip-sample separation is highlighted with purple and gold circles. d) Microscale illustration of the tip-sample system, bathed in incident IR light, at the point in time of greatest, $\tau = \tau_1$, ((e) least, $\tau = \tau_1 + T_c/2$) tip-sample separation. Note that the far-field scattering is only slightly modified by the nanoscale geometrical perturbations associated with cantilever oscillation. Panels (f) and (g) provide nanoscale Zoom-in illustrations of the previous two panels and emphasize how near-field scattering events from nanoscopic volumes below the probe tip end are highly dependent on the nanoscale geometrical perturbations associated with cantilever oscillation.

d subscript on $\boldsymbol{x}_d$ is used to emphasize that the integral is over the surface area of the detector, and the time variables are related by $t = \tau - T_d/2$. Figure 4 schematically aids in visualizing the coordinate system and described processes.

While not pictured in Figure 1, light from the reference and sample arms of the AMI (dotted yellow and blue arrows in Figure 1) is focused onto the detector with optics including another parabolic mirror. This results in the light beam incident on the detector surface having a cone-like geometry, as illustrated in Figure 4. In this work, we approximate the Poynting flux directionality at the detector surface as being solely normally incident ($\hat{\boldsymbol{x}}$ direction) to the detector surface — akin to considering the spatial average of the Poynting flux about its azimuthally symmetric beam path. Thus, we rewrite $\boldsymbol{S}(x_d, \tau, \xi)$ as $S(\tau, \xi)\hat{\boldsymbol{x}}$, and the surface integral simplifies to the product of the detector area, a and the Poynting flux evaluated at any point on the surface of the detector: $\mathbb{s}(t, \xi) = \langle \eta a S(\tau, \xi) \rangle_{T_d}$. Furthermore, because $S = |\boldsymbol{S}| = |\boldsymbol{E} \times \boldsymbol{B}| = (1/\mu_0)|\boldsymbol{E}||\boldsymbol{B}|$, and $|\boldsymbol{E}| = c|\boldsymbol{B}|$ in source

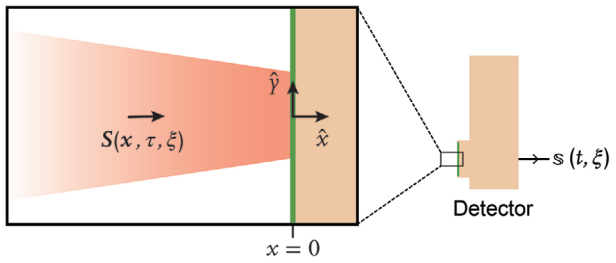

Figure 4. Schematic zoom-in of the detector surface with incident IR light.

free regions, like the region directly adjacent to the detector, the expression for the detector signal becomes

$$\mathbb{s}(t,\xi) = \frac{\eta a}{c\mu_0 T_d} \int_{t-\frac{T_d}{2}}^{t+\frac{T_d}{2}} |\boldsymbol{E}(\tau,\xi)|^2 \, d\tau + n(t) \tag{1}$$

In Equation (1), c and μ_0 are the speed of light and permeability of free space, respectively. Furthermore, $\boldsymbol{E}$ is the real-valued total vector electric field at the detector surface, generally broadband, and depends on time (τ) and effective reference mirror position (ξ): $\boldsymbol{E}(\tau,\xi) \in \mathbb{R}$. We have additionally introduced a term, $n(t)$, which serves to represent randomized noise implicit to detection or from ambient light. As described above, the electric field is comprised of a sum of nontrivial broadband fields, one from the sample arm of the AMI, $\boldsymbol{E}_{SA}$, and one from the reference arm of the AMI, $\boldsymbol{E}_{RA}$. The square of the real-valued field is $|\boldsymbol{E}|^2 = \boldsymbol{E}\cdot\boldsymbol{E} = (\boldsymbol{E}_{SA}+\boldsymbol{E}_{RA})\cdot(\boldsymbol{E}_{SA}+\boldsymbol{E}_{RA}) = \boldsymbol{E}_{SA}\cdot\boldsymbol{E}_{SA} + 2\boldsymbol{E}_{SA}\cdot\boldsymbol{E}_{RA} + \boldsymbol{E}_{RA}\cdot\boldsymbol{E}_{RA}$. Moreover, because we are detecting light far from the sources of radiation, $\boldsymbol{E}_{SA}$ and $\boldsymbol{E}_{RA}$ are considered plane waves with polarization orthogonal to $\boldsymbol{S}$.[38] In addition, for modeling simplicity, we treat all fields incident on the detector as being similarly polarized, say in the $\hat{\boldsymbol{y}}$ direction. Thus, at the detector surface, we can write, $\boldsymbol{E}_{SA} = E_{SA,y}\,\hat{\boldsymbol{y}}$ and $\boldsymbol{E}_{RA} = E_{RA,y}\,\hat{\boldsymbol{y}}$ (see Figure 4). Utilizing all these in Equation (1) for the detector signal yields

$$\mathbb{s}(t,\xi) = \frac{\eta a}{c\mu_0 T_d} \int_{t-\frac{T_d}{2}}^{t+\frac{T_d}{2}} \left[{E_{SA,y}}^2(\tau) + 2E_{SA,y}(\tau)\,E_{RA,y}(\tau,\xi) + {E_{RA,y}}^2(\tau,\xi) \right] d\tau + n(t) \tag{2}$$

We point out that the time dependence of the fields enters in two ways: field oscillations and periodic changes in the backscattered light from the sample arm (due to geometric changes at the tip-sample region from cantilever oscillations). Thus, the later time dependence arises only in $E_{SA,y}$, while the time dependence in $E_{RA,y}$ terms come solely from field oscillations. This difference is relevant and will be exploited later.

Moving forward with the calculation, we replace the real-valued field components in Equation (2) ($E_{SA,y}$ and $E_{RA,y}$) with their equivalent inverse Fourier transforms, which satisfy the Maxwell equations in free space. Such an expression, as described elsewhere,[39] takes the form

$$f(t,x) = \frac{1}{\sqrt{2\pi}} \int_{-\infty}^{\infty} \tilde{f}(\omega)\, e^{i\omega\left(\frac{x}{c}-t\right)} d\omega \tag{3}$$

where $\tilde{f}(\omega)\, e^{i\omega x/c} = \tilde{f}(\omega,x) = \mathfrak{F}_{t\to\omega} f(t,x)$ is the Fourier transform in time of $f(t,x)$, and $\tilde{f}(\omega) = \tilde{f}(\omega,0) = \mathfrak{F}_{t\to\omega} f(t,0)$ is the Fourier transform in time of $f(t,x)$ evaluated at the detector surface, and is generally complex: $\tilde{f}(\omega) = \tilde{f}(\omega,0) \in \mathbb{C}$. Using this functional form and the fact that the detector is located at $x = 0$, without loss of generality, $E_{SA,y}$ becomes

$$E_{SA,y}(\tau) = \frac{1}{\sqrt{2\pi}} \int_{-\infty}^{\infty} \tilde{E}_{SA,y}(\omega)\, e^{-i\omega\tau} d\omega \tag{4}$$

As for the field from the reference arm, $E_{RA,y}$, we account for spatial shifts arising from various RM positions, with the following replacement in Equation (3), $x \to x+\xi = 0+\xi$, giving

$$E_{RA,y}(\tau,\xi) = \frac{1}{\sqrt{2\pi}} \int_{-\infty}^{\infty} \tilde{E}_{RA,y}(\omega)\, e^{i\omega\left(\frac{\xi}{c}-\tau\right)} d\omega \tag{5}$$

Inserting the above relations for $E_{SA,y}(\tau)$ and $E_{RA,y}(\tau,\xi)$ into Equation (2), and switching the order of integration gives

$$\begin{aligned}\mathbb{s}(t,\xi) = \frac{\eta a}{2\pi c\mu_0} \Bigg[& \int_{-\infty}^{\infty}\int_{-\infty}^{\infty} \tilde{E}_{SA,y}(\omega_1)\,\tilde{E}_{SA,y}(\omega_2) \\ & \times \left\{ \frac{1}{T_d} \int_{t-\frac{T_d}{2}}^{t+\frac{T_d}{2}} e^{-i\tau(\omega_1+\omega_2)} d\tau \right\} d\omega_1\, d\omega_2 + 2\int_{-\infty}^{\infty}\int_{-\infty}^{\infty} \tilde{E}_{SA,y}(\omega_3) \\ & \times \tilde{E}_{RA,y}(\omega_4)\, e^{i\xi\frac{\omega_4}{c}} \left\{ \frac{1}{T_d} \int_{t-\frac{T_d}{2}}^{t+\frac{T_d}{2}} e^{-i\tau(\omega_3+\omega_4)} d\tau \right\} d\omega_3 d\omega_4 \\ & + \int_{-\infty}^{\infty}\int_{-\infty}^{\infty} \tilde{E}_{RA,y}(\omega_5)\,\tilde{E}_{RA,y}(\omega_6)\, e^{i\xi\left(\frac{\omega_5}{c}+\frac{\omega_6}{c}\right)} \\ & \times \left\{ \frac{1}{T_d} \int_{t-\frac{T_d}{2}}^{t+\frac{T_d}{2}} e^{-i\tau(\omega_5+\omega_6)} d\tau \right\} d\omega_5 d\omega_6 \Bigg] + n(t)\end{aligned} \tag{6}$$

where the numeric subscripts on the ω's serve to indicate they are simply integration variables. The time average integrals enclosed within curly brackets in Equation (6) have an analytic solution of a product of exponential and sinc functions: $\exp(-it\Omega_{lm})\mathrm{sinc}(T_d\Omega_{lm}2)$, where $\Omega_{lm} = \omega_l + \omega_m$ and $\mathrm{sinc}(x) = \sin(x)/x$. In the case of the time average integral in the third term, it further reduces to an effective Dirac delta distribution, as

described in Section SI.1 (Supporting Information). Incorporating these results into the above yields,

$$\mathbb{s}(t,\xi) = \mathcal{E}_{SS}(t) + \mathcal{E}_{SR}(t,\xi) + \mathcal{E}_{RR} + n(t) \tag{7}$$

where,

$$\mathcal{E}_{SS}(t) = \frac{\eta a}{2\pi c \mu_0} \int_{-\infty}^{\infty}\int_{-\infty}^{\infty} \tilde{E}_{SA,\gamma}(\omega_1)\,\tilde{E}_{SA,\gamma}(\omega_2) \times \operatorname{sinc}\left(\frac{T_d \Omega_{12}}{2}\right) e^{-i\Omega_{12}t} d\omega_1\, d\omega_2, \tag{8}$$

$$\mathcal{E}_{SR}(t,\xi) = \frac{\eta a}{\pi c \mu_0} \int_{-\infty}^{\infty}\int_{-\infty}^{\infty} \tilde{E}_{SA,\gamma}(\omega_3)\,\tilde{E}_{RA,\gamma}(\omega_4)\, e^{i\xi\frac{\omega_4}{c}} \times \operatorname{sinc}\left(\frac{T_d \Omega_{34}}{2}\right) e^{-i\Omega_{34}t} d\omega_3 d\omega_4 \tag{9}$$

and

$$\mathcal{E}_{RR} = \frac{\eta a}{2\pi c \mu_0} \int_{-\infty}^{\infty} \left|\tilde{E}_{RA,\gamma}(\omega_6)\right|^2 d\omega_6, \tag{10}$$

and $\mathcal{E}_{SS}$, $\mathcal{E}_{SR}$, and $\mathcal{E}_{RR}$, are terms for the time-averaged electromagnetic energy detected and associated with various combinations of $E_{SA,\gamma}$ and $E_{RA,\gamma}$, as denoted by the two subscripts. The so-called "self-homodyne" signal associated with coupling/interference between far-field (E^{FF}) and near-field (E^{NF}) backscattered light is contained within $\mathcal{E}_{SS}(t)$ (because $E_{SA} = E^{FF} + E^{NF}$). The so-called "heterodyne" signal associated with coupling/interference between near-field backscattered light and light from the reference arm of the AMI is contained in $\mathcal{E}_{SR}(t,\xi)$.

2.3. Expressing Detector Signal Terms as Fourier Series in Time

This section does not cover any formal step in the detection and signal process scheme. As shown in Figure 1, the next step after detector time-averaging, $\langle\cdots\rangle_{T_d}$, is lock-in amplification, $\mathfrak{L}$, which will be covered in Section 2.4. Rather, this section is focused on recasting some of the terms in Equation (7) into a form more amenable to simplification once acted on by the lock-in operator. As described in detail in Section SI.2 (Supporting Information), if the lock-in acts upon a signal that can be represented as a Fourier series in time, then calculating the result of the lock-in operation on that signal becomes straightforward. Currently, Equations (7)–(10) are decidedly not cast in terms of a Fourier series in time, and while barreling on to the lock-in operation with brute force is technically an option, it is certainly not the path of least resistance. With this knowledge, we can use the time-translation symmetry of our physical system (its known periodicity in time) to reformulate certain terms in Equation (7) as Fourier series in time and simplify the steps for the lock-in in Section 2.4.

The third term in Equation (7), $\mathcal{E}_{RR}$ (see Equation (10)), is time-independent as a result of detector time-averaging. However, the first and second terms, $\mathcal{E}_{SS}(t)$ and $\mathcal{E}_{SR}(t,\xi)$, maintain time dependence because geometrical changes associated with the oscillating AFM probe occur at order of magnitude longer time scales than the detector time averaging ($T_d \approx 1\,\mu s$ whilst $T_c \approx 10\,\mu s$). Under the reasonable assumption that the sample's local materials properties are constant — because the AFM is not in contact mode, and the IR photon energy is low — the geometrical changes are the only cause for detectible temporal changes in the electric field back-scattered from the IR-illuminated cantilever-sample system. Because the AFM cantilever is driven to oscillate with a known period, T_c, the geometrical configuration of the tip-sample system possesses the following temporal periodicity: $\boldsymbol{G}(t) = \boldsymbol{G}(t + T_c)$, where $\boldsymbol{G}(t)$ is the set of parameters that define a unique geometrical configuration. It follows that all remaining time-dependent signals will possess the same temporal periodicity: $\mathcal{E}_{SS}(t) = \mathcal{E}_{SS}(t + T_c)$ and $\mathcal{E}_{SR}(t,\xi) = \mathcal{E}_{SR}(t + T_c, \xi)$. Because $\mathcal{E}_{SS}(t)$ and $\mathcal{E}_{SR}(t,\xi)$ are real-valued and periodic in time, they can be represented as a series of orthonormal basis functions. Here we choose the cosine function with a phase, generally giving

$$\mathcal{E}_{SS}(t) = \sum_{\beta=0}^{\infty} V_\beta \cos\left(\beta\omega_c t + \varphi_\beta\right) \tag{11}$$

and

$$\mathcal{E}_{SR}(t,\xi) = \sum_{n=0}^{\infty} U_n(\xi) \cos\left(n\omega_c t + \theta_n(\xi)\right) \tag{12}$$

As mentioned at the top of this section, the motivation for casting $\mathcal{E}_{SS}(t)$ and $\mathcal{E}_{SR}(t,\xi)$ in such a series expansion is due to the forthcoming lock-in operation. Once cast as a Fourier series in time, the lock-in will transform such series into known combinations of expansion coefficients and/or phases (cf. the next section, Section SI.2, Supporting Information). Of particular interest will be the product of an expansion coefficient with the cosine of the corresponding phase, as will be shown soon. Before moving on to deriving how the expansion coefficients in the above two equations relate to the fields in Equations (8) and (9), we first explain how describing the backscattered light as a sum of far-field driven excitations (E_γ^{FF}) and near-field-driven excitations (E_γ^{NF}) influences the above equations.

The light backscattered from the tip-sample region (and measured at the IR detector) can be described as a sum of fields: $E_{SA,\gamma}(t) = E_\gamma^{FF}(t) + E_\gamma^{NF}(t)$. Thus, occurrences of $\tilde{E}_{SA,\gamma}(\omega)$ can be replaced with $\tilde{E}_\gamma^{NF}(\omega) + \tilde{E}_\gamma^{FF}(\omega)$. If we make use of this additional fact for $\mathcal{E}_{SR}(t,\xi)$ in Equation (9), algebra reveals it is actually the sum of two terms. Each of these terms still possesses the same aforementioned temporal periodicity, and thus can each also be represented with a series expansion as described before. So, Equation (12) becomes $\mathcal{E}_{SR}(t,\xi) = \mathcal{E}_{SR}^{NF}(t,\xi) + \mathcal{E}_{SR}^{FF}(t,\xi)$, and in series form is

$$\mathcal{E}_{SR}(t,\xi) = \sum_{n=0}^{\infty} u_n^{NF}(\xi) \cos\left(n\omega_c t + \theta_n^{NF}(\xi)\right) + \sum_{n=0}^{\infty} u_n^{FF}(\xi) \times \cos\left(n\omega_c t + \theta_n^{FF}(\xi)\right) \tag{13}$$

With this notation, the first series in Equation (13) is $\mathcal{E}_{SR}^{NF}(t,\xi)$, and the second series is notated as $\mathcal{E}_{SR}^{FF}(t,\xi)$. Note that we did

not apply the same algebra to $\mathcal{E}_{SS}(t)$ in Equation (11). This is because, with the benefit of foresight, contributions from $\mathcal{E}_{SS}(t)$ to the final spectra will vanish, as we will describe in Section 2.5.

One additional refinement is now needed to modify Equation (13). As already mentioned in Section 2.1, the dominant contributor to the total backscattered light is far-field scattering from microscale regions in-and-around the tip-sample region (Figure 3b,d,e); represented mathematically by the summation on the right-hand side of Equation (13) and abbreviated by $\mathcal{E}_{SR}^{FF}(t,\xi)$. This far-field scattering only very modestly changes in time with the cantilever oscillation because the nanoscopic changes in probe position are only weakly perturbative to the microscale geometry from which such scattering is occurring (Figure 3d,e). Therefore, in Equation (13), the zeroth and first harmonic terms in the Fourier expansion for the far-field signal, which constitute a constant-in-time background and simple periodic change, should be necessary and (mostly) sufficient to describe $\mathcal{E}_{SR}^{FF}(t,\xi)$ — that is, the detector time-averaged product of the reference light and far-field scattering from the tip-sample region, assuming that the cantilever is oscillating harmonically. With this, Equation (13) becomes

$$\begin{aligned}\mathcal{E}_{SR}(t,\xi) &= \mathcal{E}_{SR}^{NF}(t,\xi) + \mathcal{E}_{SR}^{FF}(t,\xi)\\ &\cong \sum_{n=0}^{\infty} u_n^{NF}(\xi)\cos\left(n\omega_c t + \theta_n^{NF}(\xi)\right)\\ &+ \sum_{n=0}^{1} u_n^{FF}(\xi)\cos\left(n\omega_c t + \theta_n^{FF}(\xi)\right)\end{aligned} \tag{14}$$

Now having finished incorporating the near- and far-field contributions explicitly, the last step in this section is to derive expressions that relate the expansion coefficients and phases in Equation (14) to the fields in Equation (9). Again, this is because of the upcoming lock-in amplification on $\mathcal{E}_{SR}(t,\xi)$ will produce terms that are a product between expansion coefficient and the cosine of the corresponding phase (see Section SI.2, Supporting Information). Analytically solving for such expressions is done by utilizing cosine orthogonality relations, and limiting cases of the sinc function, and is explicitly derived in Section SI.3 (Supporting Information). The results are

$$\begin{aligned}u_n^{NF}(\xi)\cos\left(\theta_n^{NF}(\xi)\right) &= \mathcal{J}\int_{-\infty}^{\infty}\left[\tilde{E}_y^{NF^*}(\omega-n\omega_c)+\tilde{E}_y^{NF^*}(\omega+n\omega_c)\right]\\ &\times \tilde{E}_{RA,y}(\omega)\,e^{i\xi\frac{\omega}{c}}d\omega\end{aligned} \tag{15}$$

$$\begin{aligned}u_{n\le 1}^{FF}(\xi)\cos\left(\theta_{n\le 1}^{FF}(\xi)\right) &= \mathcal{J}\int_{-\infty}^{\infty}\left[\tilde{E}_y^{FF^*}(\omega-n\omega_c)+\tilde{E}_y^{FF^*}(\omega+n\omega_c)\right]\\ &\times \tilde{E}_{RA,y}(\omega)\,e^{i\xi\frac{\omega}{c}}d\omega\end{aligned} \tag{16}$$

$$u_{n>1}^{FF}(\xi)\cos\left(\theta_{n>1}^{FF}(\xi)\right) \cong 0 \tag{17}$$

and where $\mathcal{J} = \eta a\,\mathrm{sinc}(T_a n\omega_c/2)/(\pi c\mu_0)$,

and, now being armed with a signal whose terms of interest are cast as Fourier series in time, and with knowledge of how the generalized fields relate to the expansion coefficients in those series, we are prepared to move to the lock-in amplification step of the detection and signal processing scheme.

2.4. Lock-In Amplification $\mathfrak{L}$: Removal of Constant Terms and Time Dependence, Suppression of Noise, Isolation of Fourier Expansion Coefficients, and Formation of the Interferogram

Lock-in amplification is a process of performing two real-valued transformations on a polluted signal to extract information of interest. The polluted signal is typically a sum of a perfectly periodic function of interest, unwanted information, and noise. By time-averaging the product of the polluted signal and a cosine or sine function (with an integer multiple of the frequency of interest), Fourier expansion coefficients that describe the embedded and obscured periodic function of interest can be isolated. This process typically also removes time dependence. It is common to think of the two real-valued transformations as one complex transformation that maps the single real signal to a complex signal whose real (imaginary) part is defined as the time average of the signal multiplied by cosine (sine). Because of this, it is common for lock-in amplifiers to output this defined complex signal. Following this convention, we herein denote the linear operator of the single complex lock-in operation as $\mathfrak{L}_m$, where m is a positive integer that defines the "harmonic" being considered. A detailed accounting of all the essential mathematical steps that the lock-in effectively performs is provided in Section SI.2 (Supporting Information).

The next step is to calculate $\mathfrak{L}_m\mathbb{s}(t,\xi)$. As the reference mirror translates, data is output from the lock-in and recorded as a function of effective mirror position ξ. The ξ-dependent real and imaginary outputs of the lock-in constitute the complex-valued interferogram: $\mathfrak{L}_m\mathbb{s}(t,\xi) \equiv I_m(\xi) = I'_m(\xi) + iI''_m(\xi)$. In passing, we caution the reader not to confuse the real and imaginary (or amplitude and phase) lock-in outputs, which define the complex-valued interferogram, with the real and imaginary components (or the amplitude and phase) of the complex-valued normalized nano-FTIR spectrum, which is still yet to be constructed.

As described in detail in Section SI.2 (Supporting Information), the lock-in operation will cause two kinds of terms to vanish: those that are constant-in-time, and those that are randomized noise and non-monotonically increasing or decreasing. Therefore, as $\mathfrak{L}_m$ is applied to Equation (7), $\mathfrak{L}_m\mathcal{E}_{RR} = \mathfrak{L}_m n(t) = 0$, leaving $\mathfrak{L}_m\mathbb{s}(t,\xi) = \mathfrak{L}_m\mathcal{E}_{SS}(t) + \mathfrak{L}_m\mathcal{E}_{SR}(t,\xi)$. Because $\mathcal{E}_{SS}(t)$ and $\mathcal{E}_{SR}(t,\xi)$ can be expressed as sums of cosines (Equations 11 and 14), and for details outlined in Section SI.2 (Supporting Information), $\mathfrak{L}_m\mathbb{s}(t,\xi)$ reduces to the following (where we have allowed the general index $m \to n$):

$$\begin{aligned}I_n(\xi) = &\frac{V_n\cos(\varphi_n)}{2} + \frac{u_n^{NF}(\xi)\cos\left(\theta_n^{NF}(\xi)\right)}{2}\\ &+ \frac{u_n^{FF}(\xi)\cos\left(\theta_n^{FF}(\xi)\right)}{2} + i\left\{\frac{V_n\sin(\varphi_n)}{2}\right.\\ &\left.+ \frac{u_n^{NF}(\xi)\sin\left(\theta_n^{NF}(\xi)\right)}{2} + \frac{u_n^{FF}(\xi)\sin\left(\theta_n^{FF}(\xi)\right)}{2}\right\}\end{aligned} \tag{18}$$

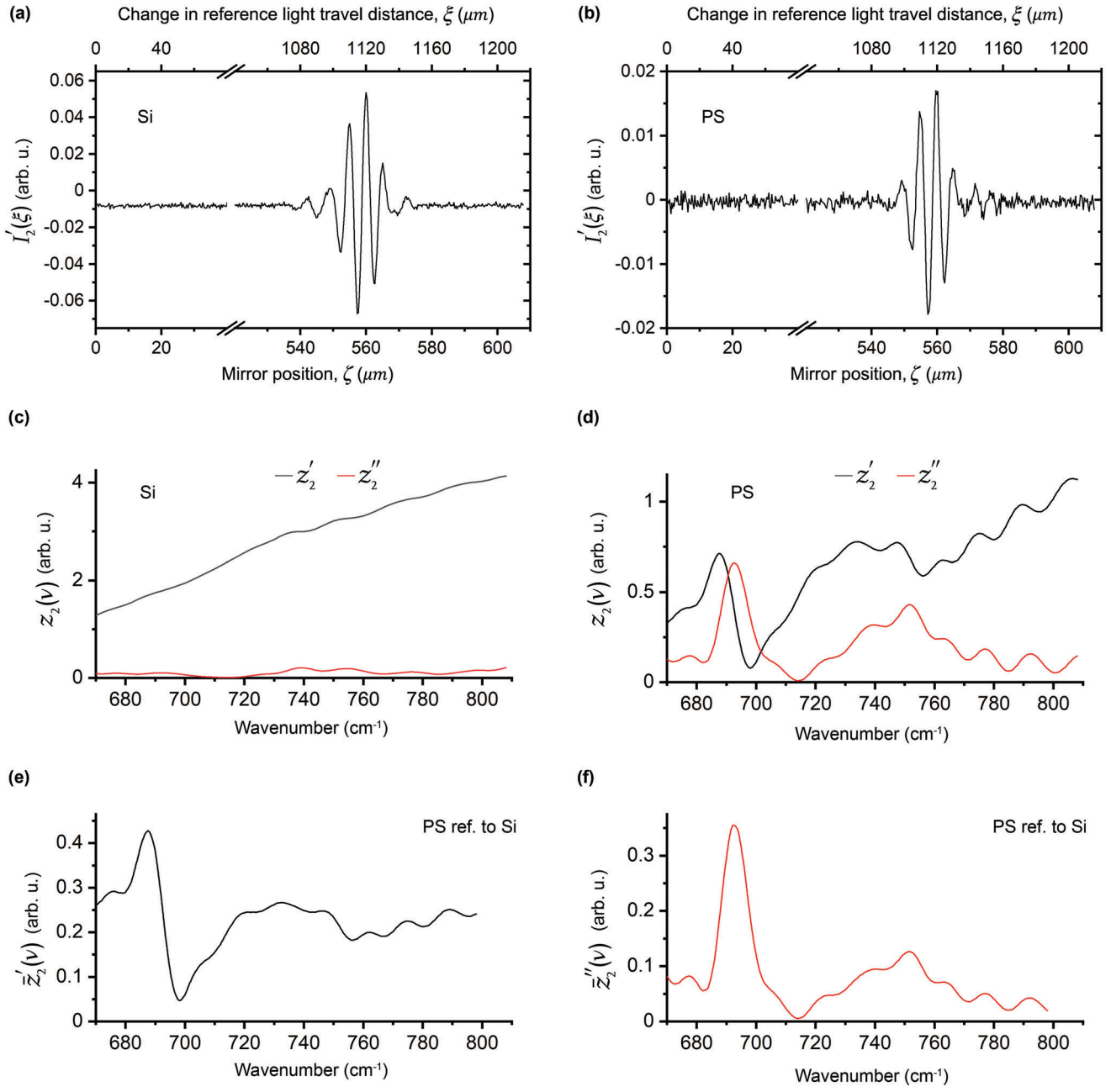

Figure 5. Representative key data sets in the generation of a normalized complex valued nano-FTIR spectrum. Panels (a) and (b) are second harmonic nano-FTIR interferograms for Si and PS respectively. Panels (c) and (d) are plots of the real and imaginary parts of the Fourier transform of the interferograms ($z_2 = \mathfrak{F}_{\xi\to\nu} I_2'$) for Si and PS respectively. Panels (e) and (f) are, respectively, the real and imaginary parts of the second harmonic of the complex-valued nano-FTIR spectrum of PS referenced to Si: $\bar{z}_2 = \mathfrak{N} z_2^{\mathrm{PS}} = z_2^{\mathrm{PS}}/z_2^{\mathrm{Si}}$. Note that the former possesses dispersion-like features, while the latter possesses absorption-like features.

Here, $I_n(\xi)$ is the time-independent complex valued interferogram of the nth harmonic. The real part of this quantity, $I_n'(\xi)$, is coined the interferogram of the nth harmonic and is the critical ξ-dependent signal that is passed onto a computer for further processing (Figure 1). As an example, interferograms of the second harmonic for Si and polystyrene (PS) are provided in **Figure 5**a,b respectively. Before moving further along, we note in passing that the time-averaging period for the lock-in, $T_L = 10^{-4}$ s = 100 μs, is an order of magnitude larger than the cantilever period; and so, each lock-in data point output is a time average over roughly ten cantilever oscillations.

At this point, it is reasonable to pause and address a likely question: what is the difference between the complex interferograms of various harmonics (different values for n)? For reasons recently described above Equation (14), for the zeroth and fundamental harmonics, $n \leq 1$, backscattering will be dominated

by contributions from far-field scattering. Thus, $I_{n\leq 1}(\xi)$ is a complex interferogram with predominantly far-field scattering information encoded in it. On the other hand, when $n > 1$, far-field contributions diminish, especially those from the heterodyne term (Equations 14 and 17), and the complex interferogram $I_{n>1}(\xi)$ has a significantly greater proportion of near-field scattering information encoded in it relative to $n \leq 1$:

$$I_{n>1}(\xi) = \frac{V_n \cos(\varphi_n)}{2} + \frac{u_n^{NF}(\xi)\cos\left(\theta_n^{NF}(\xi)\right)}{2} + i\left\{\frac{V_n \sin(\varphi_n)}{2} + \frac{u_n^{NF}(\xi)\sin\left(\theta_n^{NF}(\xi)\right)}{2}\right\} \quad (19)$$

For these reasons, nano-FTIR experiments focus on lock-in harmonics two and higher, to isolate near-field contributions. In the following expressions, we will do the same.

2.5. Fourier Transformation $\mathfrak{F}$: Removal of Self-Homodyne Background and Generation of the Unnormalized Complex-Valued Spectrum

As shown in Figure 1 and described above, the interferogram $I'_{n>1}(\xi)$ (the real part of the complex valued interferogram) is passed along to a computer for further processing where Fourier transformation (FT) and normalization occur. Thus, the next computation step is to conduct the relevant FT: $\mathfrak{F}_{\xi\to\nu} I'_{n>1}(\xi)$, where $\mathfrak{F}_{\xi\to\nu}$ is the operator for FT and for some function of ξ, say $p(\xi)$, the FT is here defined as

$$\mathfrak{F}_{\xi\to\nu} p(\xi) = \int_{-\infty}^{\infty} \left\{p(\xi_1)\, e^{i2\pi\nu\xi_1}\right\} d\xi_1 \quad (20)$$

Note that the choice of passing on the $I'_{n>1}(\xi)$ for FT is not the only way to proceed, as the desired information is ultimately captured in $u_n^{NF}(\xi)\cos(\theta_n^{NF}(\xi))$ and $u_n^{NF}(\xi)\sin(\theta_n^{NF}(\xi))$, which are contained in the real and imaginary parts of the complex-valued interferogram respectively. We chose the real part herein for the convention.

Ultimately, the FT operation will i) remove the self-homodyne background signal (terms proportional to expansion coefficients V_n that contain interference/coupling between E^{FF} and E^{NF}), ii) change the independent variable from ξ to wavenumber "ν," and iii) generate the unnormalized complex valued nano-FTIR spectrum. Because the FT operation on a constant is known to produce a Dirac delta distribution, and because the first term in the real part of complex interferogram (Equation 19) is independent of ξ, that term vanishes for non-zero wavenumbers; and so, the self-homodyne background vanishes. This leaves behind the FT of the second term in $I'_{n>1}(\xi)$:

$$z_{n>1}(\nu) \equiv \mathfrak{F}_{\xi\to\nu} I'_{n>1}(\xi) = \mathfrak{F}_{\xi\to\nu} \frac{u_n^{NF}(\xi)\cos\left(\theta_n^{NF}(\xi)\right)}{2} \quad (21)$$

where $z_{n>1}(\nu)$ is here defined as the raw, unnormalized, and complex-valued nano-FTIR spectrum. Examples of the real and imaginary parts of the raw, unnormalized, and complex-valued nano-FTIR spectrum (second harmonic) for Si and PS are plotted in Figure 5c and 5d respectively. We note that while in this work we focus on an analytical/continuum model for the detection and signal processing, which for FT is a straightforward integral as in Equation (20), in practice, some additional numerical data processing of the interferogram is usually involved, as is common with conventional FTIR, including the likes of zero filling, apodization, etc.; the interested reader can look to the literature to learn more about these numerical steps.[1b,5f,40]

Now, we can move to compute the complex nano-FTIR spectrum in terms of the fields by introducing Equation (15) into (21); and a change of integration order yields

$$z_{n>1}(\nu) = \frac{\eta a \,\mathrm{sinc}\left(\frac{T_d n\omega_c}{2}\right)}{2\pi c\mu_0} \int_{-\infty}^{\infty} \left[\tilde{E}_y^{NF*}(\omega - n\omega_c) + \tilde{E}_y^{NF*}(\omega + n\omega_c)\right] \times \tilde{E}_{RA,y}(\omega) \int_{-\infty}^{\infty} e^{i\xi_1\left(\frac{\omega}{c}+2\pi\nu\right)} d\xi_1 d\omega, \quad (22)$$

which simplifies to

$$z_{n>1}(\nu) = \Gamma_n \left[\tilde{E}_y^{NF}(2\pi\nu c + n\omega_c) + \tilde{E}_y^{NF}(2\pi\nu c - n\omega_c)\right] \times \tilde{E}^*_{RA,y}(2\pi\nu c) \quad (23)$$

where $\Gamma_n = 2\eta a\ \mathrm{sinc}(T_d n\omega_c/2)/(c\mu_0)$. The simplification process to arrive at Equation (23) included i) the integral over ξ_1 reducing to a Dirac delta distribution which demanded $\omega \to -2\pi\nu c$, and ii) the use of the reality condition that if $f(t)$ is real-valued, $\tilde{f}^*(-\omega) = \tilde{f}(\omega)$.

2.6. Normalization $\mathfrak{N}$: Removal of Scaled Reference Arm Light and Arrival at the Normalized Complex-Valued Spectrum

The last processing step is normalization. As can be seen in Equation (23), an unnormalized nano-FTIR spectrum is linearly proportional to $\Gamma_n \tilde{E}^*_{RA,y}(2\pi\nu c)$. To remove these, a normalization strategy is employed. Two nano-FTIR spectra are collected, one of the sample material of interest, and another of a reference material with constant-in-ν (or smoothly varying) dielectric properties. Then, a ratio of the two spectra is taken, and the $\Gamma_n \tilde{E}^*_{RA,y}(2\pi\nu c)$ terms in the numerator and denominator cancel as both reference field and prefactor Γ_n do not change between measurements. Thus, in general, a normalized complex valued nano-FTIR spectrum, $\mathfrak{N} z_{n>1}(\nu) = \bar{z}_{n>1}(\nu)$, will take the form,

$$\bar{z}_{n>1}(\nu) \equiv \frac{z_{n>1}^{t\&sm}(\nu)}{z_{n>1}^{t\&rm}(\nu)} = \frac{\tilde{E}_y^{NF,t\&sm}(\omega_n^+(\nu)) + \tilde{E}_y^{NF,t\&sm}(\omega_n^-(\nu))}{\tilde{E}_y^{NF,t\&rm}(\omega_n^+(\nu)) + \tilde{E}_y^{NF,t\&rm}(\omega_n^-(\nu))} \quad (24)$$

where superscripts "*t&sm*" and "*t&rm*" stand for "tip and sample material" and "tip and reference material," respectively, and $\omega_n^{\pm}(\nu) = 2\pi\nu c \pm n\omega_c$. Also, as mentioned earlier, a "good" reference material has known dielectric properties and is spectrally flat, having no absorption resonances within the wavenumber region of interest. Common reference materials are gold or silicon

— though, because of the importance of references, recent work has been aimed at developing standardized reference samples.[41] So, to provide a concrete example, if the material of interest was PS, the reference material was Si, and n was two, a thorough way to refer to such a case would be "the second harmonic of the complex-valued nano-FTIR spectrum of PS referenced to Si." The real and imaginary parts of this spectrum, $\bar{z}_2'(\nu)$ and $\bar{z}_2''(\nu)$, are plotted in Figure 5e and 5f respectively.

Equation (24) can also be cast in terms of the FT of the product of $E_y^{NF}(t)$ and $\cos(n\omega_c t)$:

$$\bar{z}_{n>1}(\nu) = \frac{z_{n>1}^{t\&sm}(\nu)}{z_{n>1}^{t\&rm}(\nu)} = \frac{\mathfrak{F}_{t\to\omega(\nu)}\left[E_y^{NF,t\&sm}(t)\cos\left(n\omega_c t\right)\right]}{\mathfrak{F}_{t\to\omega(\nu)}\left[E_y^{NF,t\&rm}(t)\cos\left(n\omega_c t\right)\right]} \tag{25}$$

In principle, the right-hand side of either Equation (24) or (25) can be used as a springboard for inputting one's favorite near-field scattering model. This would be done, of course, with the aim to establish relationships between the sample material's local properties, and the real and imaginary parts of $\bar{z}_{n>1}(\nu)$, which are measured. Here, in their current forms, they lack explicit dependence on physical quantities that are associated with, or reside in, the tip-sample region. We address this in the following section. However, before we do so, we would like to draw a clear connection to past works. If the sums of frequency-shifted FT fields appearing in the numerator and denominator of Equation (24) can be approximated as two times the FT field itself, $\tilde{E}_y^{NF}(\omega_n^+) + \tilde{E}_y^{NF}(\omega_n^-) \approx 2\tilde{E}_y^{NF}(\omega; n)$, one retrieves a similar modeling starting point used in other works. In particular, a ratio of FT fields backscattered from the tip-sample region: $\bar{z}_{n>1} = E_{n,s}/E_{n,ref} = \sigma_{n,s}/\sigma_{n,ref}$.[5c,13a] We note that, to our knowledge, this work is the first that explicitly highlights these frequency shifts (Equation 24) within the context of nano-FTIR detection and signal processing, and that they are likely relevant when attempting to extract quantitative materials property information out of $\bar{z}_{n>1}$ with modeling.

2.7. Casting the Normalized Complex-Valued Spectrum in Terms of Radiation from a Generalized Dipole with Nanoscale Volume

Now that the detection and signal processing steps for scattering-type near-field infrared nanospectroscopy have been fully modeled, we aim to move toward interpretation. This requires casting $\tilde{E}_y^{NF}(\omega) = \tilde{E}_y^{NF}(\omega, x = 0)$, a quantity physically located at the detector surface, in terms of quantities within the tip-sample region. For this reason, we first define new cartesian and polar coordinate systems that more directly relate to the scattering problem, and whose origin is the center of the tip-sample region at minimum tip-sample separation, as shown in **Figure 6**.

Because i) the detector is physically located at a much larger distance (R) than the characteristic size (l) of the charges accelerating due to near-field excitations (they are confined to nanoscopic volumes in the tip-sample region), ii) the wavelength of the incident IR light is also much larger than l, and iii) $R \gg \lambda \gg l$, dipole radiation[38,39,42] from the tip-sample region is what constitutes $\tilde{E}_y^{NF}(\omega, x = 0)$. Thus, we draw (as a blue arrow in Figure 6) an effective net dipole moment, of the whole tip-sample region as would be "seen" a far distance away. From symmetry,

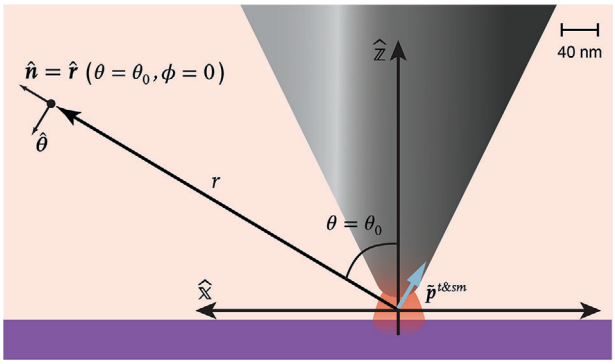

Figure 6. Schematic of the tip-sample region.

we infer the dipole moment should be confined to the $\mathbb{x}/\mathbb{z}$ plane because the incident polarization is primarily in the $\mathbb{x}/\mathbb{z}$ plane. The mathematical relationship between the coordinate systems can be expressed as

$$\tilde{E}_y^{NF}(\omega, x = 0) = \tilde{E}_\theta^{NF}\left(\omega, r = R, \theta = \theta_0, \phi = 0\right) g(\omega) \tag{26}$$

where R is the fixed distance between the tip-sample region and the detector, θ_0 is the fixed angle between the polar axis ($\hat{\mathbb{z}}$ in Figure 6) and the fixed backscattering direction $\hat{\boldsymbol{n}} = \hat{\boldsymbol{r}}\ (\theta_0, 0)$ (see Figure 6), and $g(\omega)$ is a correction factor which accounts for influences that the optics of the sample arm of the AMI may have on the backscattered light as it travels toward the detector. Furthermore, generalized dipole radiation fields are well-known in terms of the FTs in time.[39,42] For the case outlined above, this vector expression is $(-\omega^2\mu_0 Exp[i\omega r/c](\tilde{\boldsymbol{p}} \times \hat{\boldsymbol{n}}) \times \hat{\boldsymbol{n}}))/(4\pi R)$, it reduces to a vector expression having only a $\hat{\boldsymbol{\theta}}$ component. In particular,

$$\tilde{E}_\theta^{NF}\left(\omega, r = R, \theta = \theta_0, \phi = 0\right) = \frac{-\omega^2\mu_0 e^{\frac{i\omega R}{c}}}{4\pi R} \times \left(-\tilde{p}_{\mathbb{x}}(\omega)\cos\left[\theta_0\right] + \tilde{p}_{\mathbb{z}}(\omega)\sin\left[\theta_0\right]\right) \tag{27}$$

where $\tilde{p}_{\mathbb{x}}$ and $\tilde{p}_{\mathbb{z}}$ are the vector components of $\tilde{\boldsymbol{p}}$.

With Equation (26) and (27) input into (24), and with reasonable algebraic simplifications outlined in Section SI.4 (Supporting Information), the normalized complex-valued spectrum becomes

$$\bar{z}_{n>1}(\nu) = \frac{\left(\frac{n\omega_c}{\omega}\right)^0 \Delta_+^{t\&sm} + \left(\frac{n\omega_c}{\omega}\right)^1 2\Delta_-^{t\&sm} + \left(\frac{n\omega_c}{\omega}\right)^2 \Delta_+^{t\&sm}}{\left(\frac{n\omega_c}{\omega}\right)^0 \Delta_+^{t\&rm} + \left(\frac{n\omega_c}{\omega}\right)^1 2\Delta_-^{t\&rm} + \left(\frac{n\omega_c}{\omega}\right)^2 \Delta_+^{t\&rm}} \tag{28}$$

where,

$$\Delta_\pm^j = \frac{\mathcal{D}^j\left(\omega + n\omega_c\right) \pm \mathcal{D}^j\left(\omega - n\omega_c\right)}{2n\omega_c}, \tag{29}$$

and

$$\mathcal{D}^j(\omega) = e^{\frac{i\omega R}{c}}\, g(\omega)\left(-\tilde{p}_{\mathbb{x}}^j(\omega)\cot\left[\theta_0\right] + \tilde{p}_{\mathbb{z}}^j(\omega)\right) \tag{30}$$

or,

$$\mathcal{D}^j(\omega) = e^{\frac{i\omega R}{c}}\, g(\omega)\, \varepsilon_0 \left(-\int_V \left(\varepsilon_r(\omega) - 1\right) \tilde{E}^j_{\mathbb{x}}(\omega, \boldsymbol{r})\, dV \cot\left[\theta_0\right] + \int_V \left(\varepsilon_r(\omega) - 1\right) \tilde{E}^j_{\mathbb{z}}(\omega, \boldsymbol{r})\, dV \right) \tag{31}$$

The derivation of Equation (31) makes use of a relation derived and supplied in Section SI.5 (Supporting Information), $\tilde{\boldsymbol{p}}(\omega) = \varepsilon_0 \int_V (\varepsilon_r(\omega) - 1)\tilde{\boldsymbol{E}}\, d^3V$, which relates the FT of the dipole moment of an arbitrary charge distribution to the charge distribution's relative dielectric permittivity and the integral of the FT of the field over the volume of the distribution. Thus, as integrals are taken over either tip or sample volumes, the dielectric function will change accordingly. Furthermore, if the dielectric properties are not isotropic, ε_r can be readily replaced with either $\varepsilon_{\mathbb{x}}$ or $\varepsilon_{\mathbb{z}}$. Superscripts on $\mathcal{D}^j$ and $\Delta^j_\pm$ take one of the two already defined notations of $j = t\&sm$ or $t\&rm$ and we stop explicitly notating the functional dependence of ω on ν (treating this as understood).

With this, we have finally cast the normalized spectrum in terms of clear-cut (though yet undetermined) physical quantities associated with the tip-sample region, $\tilde{p}_{\mathbb{x}}$ and $\tilde{p}_{\mathbb{z}}$, or ε_r with $\tilde{E}_{\mathbb{x}}$ and $\tilde{E}_{\mathbb{z}}$, which can be modeled as one sees fit. As currently expressed, each of the three terms in the numerator (and denominator) of the normalized complex-valued spectrum are scaled by a small dimensionless multiplicative prefactor, raised to various powers (say of q): $(n\omega_c/\omega_{IR})^q$. For the system at hand, $10^{-9} \lesssim (n\omega_c/\omega) \lesssim 10^{-8}$. Therefore, the power q of the prefactor defines each term's relative degree of smallness: zeroth order in smallness ($q = 0$), first order in smallness ($q = 1$), and second order in smallness ($q = 2$). We additionally mention that each of the $\Delta^j_\pm$ terms in Equations (28) and (29), with a judicious use of Taylor series expansions, can be approximated as a series that contains various orders of derivatives involving the dipole moments. That said, such pursuits toward ultimate numerical precision are beyond the scope of this present work but are highly likely to be relevant in situations attempting to quantify materials' dielectric properties in a rigorous way, especially when considering strong resonances.

Equation (28), supported by Equations (29)–(31), should be considered a robust springboard/starting point for quantitative modeling of normalized spectra empirically collected. We emphasize that at this stage we have made no assumptions of any kind as to functional forms of the dipole or field terms in $\mathcal{D}$, they are strictly general expressions and can accommodate any number of models. To extract specific information about the sample material's local properties, "all" that needs to be done is the following. First, choose by order of smallness which terms in Equation (28) to keep. Second, for the terms that remain, generate and input models for the quantities on the right-hand side of Equation (28). These models will generally be complex-valued, as expressions on the right-hand side of Equation (28) depend on frequency-dependent FTs and complex exponentials. Third, equate the real and imaginary parts of the model to the corresponding empirical data on the left-hand side of Equation (28) (symbolized by $\bar{z}_{n>1}(\nu)$). Lastly, choose an appropriate method, for each frequency value, to solve the system of two equations for two unknown model parameters of interest (taking care to implement complex division where necessary); these parameters are usually the real and imaginary parts of the sample's dielectric function, $\varepsilon^{sm}_r = \varepsilon^{sm'}_r + i\varepsilon^{sm''}_r$.

2.8. Considering Detected Radiation as Originating Primarily from a Net Dipole Radiator Oriented Parallel to the Probe Axis

Usually, contributions from dipoles oriented parallel to the sample surface ($\tilde{p}_{\mathbb{x}}$) are excluded in literature analyses, as their contributions to the detected radiation, though non-zero, can be small in comparison to those originating from $\tilde{p}_{\mathbb{z}}$.[43] In light of this, and in keeping with our move toward gaining a qualitative interpretation of $\bar{z}_{n>1}$, we drop dipoles with $\mathbb{x}$ dependence from consideration. In such a case, the FT of the dipole moment shown in Figure 6 will align with the polar axis $\hat{\mathbb{z}}$, and $\mathbb{x}$-dependent terms vanish in $\mathcal{D}^j(\omega)$ occurrences in Equations (28) – (31). Additionally, we will consider two more simplifications. First, we point out that $n\omega_c R/c \approx 10^{-2}$ for the system at hand, and so the complex exponential prefactors of each term in the numerator and denominator of Equation (28) will cancel because $\exp[i\omega^\pm_n R/c] \approx \exp[i\omega R/c]$. Second, we consider that optical component influences on the backscattered light only weakly change with ω, and so $g(\omega^\pm_n) \to g(\omega)$. Application of these lead to Equation (28) – (31) simplifying to

$$\bar{z}_{n>1}(\nu) = \frac{\left(\frac{n\omega_c}{\omega}\right)^0 \delta^{t\&sm}_+ + \left(\frac{n\omega_c}{\omega}\right)^1 2\,\delta^{t\&sm}_- + \left(\frac{n\omega_c}{\omega}\right)^2 \delta^{t\&sm}_+}{\left(\frac{n\omega_c}{\omega}\right)^0 \delta^{t\&rm}_+ + \left(\frac{n\omega_c}{\omega}\right)^1 2\,\delta^{t\&rm}_- + \left(\frac{n\omega_c}{\omega}\right)^2 \delta^{t\&rm}_+} \tag{32}$$

with,

$$\delta^j_\pm = \frac{\tilde{p}^j_{\mathbb{z}}(\omega + n\omega_c) \pm \tilde{p}^j_{\mathbb{z}}(\omega - n\omega_c)}{2n\omega_c} \tag{33}$$

or,

$$\delta^j_\pm(\omega) = \frac{\varepsilon_0}{2n\omega_c} \int_V \left[\varepsilon_r(\omega^+_n) - 1\right] \tilde{E}^j_{\mathbb{z}}(\omega^+_n, \boldsymbol{r})\, dV \pm \frac{\varepsilon_0}{2n\omega_c} \int_V \left[\varepsilon_r(\omega^-_n) - 1\right] \tilde{E}^j_{\mathbb{z}}(\omega^-_n, \boldsymbol{r})\, dV \tag{34}$$

Equation (32) is as fully applicable as (28), so long as only a $\mathbb{z}$-component radiator needs to be considered, and the optical components influence the backscattered light weakly: $g(\omega^\pm_n) \to g(\omega)$. Note also in Equation (34) that we made use of $\omega^\pm_n = \omega \pm n\omega_c$ again, as a space saver in the definition of $\delta^j_\pm$.

Next, we point out that the FT of the net dipole of the tip-sample region, $\tilde{\boldsymbol{p}} = \tilde{p}^{t\&sm}_{\mathbb{z}}\, \hat{\mathbb{z}}$, can generally be found with a volume integral of the $\mathbb{z}$-component of the polarization density: $\tilde{p}^{t\&sm}_{\mathbb{z}} = \int_V \tilde{P}_{\mathbb{z}} dV$ (see **Figure 7a**). We note that a rigid definition of the exact integration volume is not needed for our purposes here, though, of course, strict boundary definitions would be required for rigorous modeling of the scattering. We here sketch a

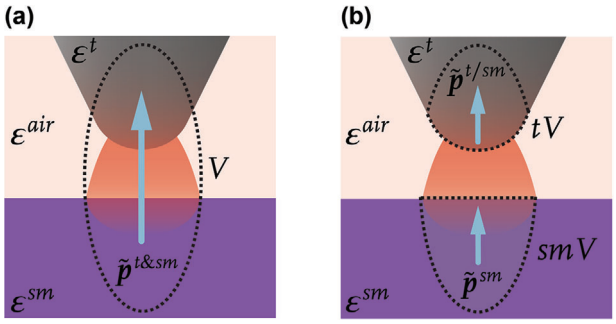

Figure 7. Equivalent schematics/representations of the tip-sample region as perceived by an observer far away from the accelerating charges. Dielectric permittivity is appropriately labeled. a) The net dipole moment induced within the volume V by the enclosed charge distributions being subjugated to near-field excitations. b) Two dipole moments induced within distinct volumes, tV and smV, arising from the enclosed charge distributions being subjugated to near-field excitations (and dipole–dipole coupling).

qualitative representative outline of a boundary for such a volume and the related net dipole along the z axis, as shown in Figure 7a.

Without loss of generality, the single integral over V can be replaced by three volume integrals. One for each material: $\tilde{p}_z^{t\&sm} = \int_V \tilde{P}_z dV = \int_{tV} \tilde{P}_z dV + \int_{air} \tilde{P}_z dV + \int_{smV} \tilde{P}_z dV$, where tV stands for the tip volume, air stands for the air gap between the probe tip and sample, and smV stands for sample material volume. Because the air in the tip-sample gap does not polarize, that integral vanishes, leaving $\tilde{p}_z^{t\&sm} = \int_{tV} \tilde{P}_z dV + \int_{smV} \tilde{P}_z dV = \tilde{p}_z^{t/sm} + \tilde{p}_z^{sm}$, and each remaining integral result, respectively, constitutes $\tilde{\boldsymbol{p}}^{t/sm} = \tilde{p}_z^{t/sm}\hat{\mathbf{z}}$ and $\tilde{\boldsymbol{p}}^{sm} = \tilde{p}_z^{sm}\hat{\mathbf{z}}$ (as shown in Figure 7b). Thus, $\tilde{\boldsymbol{p}} = \tilde{\boldsymbol{p}}^{t/sm} + \tilde{\boldsymbol{p}}^{sm}$, and $\tilde{p}_z^{t\&sm} = \tilde{p}_z^{t/sm} + \tilde{p}_z^{sm}$. Being able to separate out these two contributors to the net dipole moment is important for a holistic understanding, but also for developing detailed models which aim to account for dipole–dipole coupling through the electric field. Since the detection and signal processing theory at this stage is now complete, and with Equations (28)–(31) describing the normalized spectrum allowing for dipoles oriented both in and out of the sample surface's plane, and Equations (32)–(34) specializing to the case of net dipole/dipoles oriented out of the sample surface's plane, and parallel to the probe axis, we move toward the last goal of this work: deriving a basic, yet practically useful, interpretation of $\bar{z}_{n>1}$.

2.9. Approximating the Complex-Valued Nano-FTIR Spectrum of Weak Molecular Vibrations in a Nonmetal Sample Normalized with a Nonmetal Reference

Perhaps the most common application of nano-FTIR is to conduct vibrational spectroscopy of insulating or semiconducting materials (nonmetals). This common class of measurements, aimed at identifying chemistry and other physicochemical properties, benefits from being able to compare nano-FTIR spectra with other conventional FTIR measurements for data interpretation. This process hinges on having a basic understanding of what $\bar{z}_{n>1}(\nu)$ physically represents. In this section, we provide a semiquantitative description of what $\bar{z}_{n>1}(\nu)$ approximately represents in the case of bulk nonmetal samples and references.

We treat the net dipole as being oriented parallel to the probe axis (z axis in Figure 6), as was the case in the last section. Furthermore, we consider an ideal case in which the sample material, reference material, and probe tip are optically isotropic; that is, we assume the dielectric function of all materials only depends on scalar frequency (ν or ω). With this in mind, we now move to approximate Equation (32) by i) only keeping terms to zeroth order in smalless ($q = 0$), ii) allowing $\tilde{p}_z^j(\omega + n\omega_c) + \tilde{p}_z^j(\omega - n\omega_c) \cong 2\tilde{p}_z^j(\omega)$ (strictly valid only when the second derivate is small), and iii) replacing the single net dipole with two distinct dipoles (as described in the previous section and pictorially represented in Figure 7b); which yields

$$\bar{z}_{n>1} \cong \frac{\tilde{p}_z^{t/sm} + \tilde{p}_z^{sm}}{\tilde{p}_z^{t/rm} + \tilde{p}_z^{rm}} \tag{35}$$

The superscript notation t/sm serves to indicate "tip adjacent to sample material" and similarly, t/rm indicates "tip adjacent to reference material." Equation (35) shows that the normalized complex valued nano-FTIR spectrum is dominated by a ratio (generally complex division) of the FT of the net dipole moment of the tip-sample region to that of the FT of the net dipole moment of the tip-reference material region.

Next, we again use the general relation for the FT of an arbitrary dipole moment (derived in Section SI.5, Supporting Information). This yields

$$\bar{z}_{n>1} \cong \frac{\int_{tV} \tilde{E}_{z,in}^{t/sm} dV + \left(\frac{\epsilon_r^{sm} - 1}{\epsilon_r^{t} - 1}\right) Q_V^{sm}}{\int_{tV} \tilde{E}_{z,in}^{t/rm} dV + \left(\frac{\epsilon_r^{rm} - 1}{\epsilon_r^{t} - 1}\right) Q_V^{rm}} \tag{36}$$

however, since the probe tip is considered a very good conductor, and if we treat cases where the sample and reference materials are both nonmetallic, then the ratio in front of the second term in both the numerator and denominator is very small. Thus, we only need treat the first term in the numerator and denominator in (36): $\bar{z}_{n>1} \cong Q_{tV}^{t/sm}/Q_{tV}^{t/rm}$ where Q is an integral of the FT of the electric field component parallel to the probe axis, over the region and material referred to by the sub- and superscripts (the mathematical form is a manifestation of the fact that a metallic tip will generally backscatter much more light than a nonmetallic sample, and so radiation originating from the tip's dipole dominates the detected signal). Still, a more advantageous form can be found. To do so, we treat the tip end as a sphere being polarized by both the incident IR light and the near electric field arising from the induced dipole moment in the sample. Additionally, the volume integral of the z component of the FT of the electric field inside the sample and reference materials are approximated as smoothly varying in energy so that

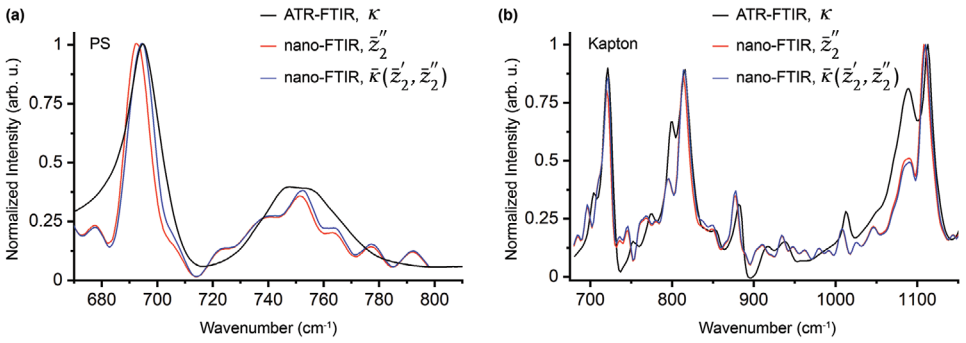

Figure 8. ATR-FTIR, nano-FTIR, and $\kappa_2(\bar{z}_2', \bar{z}_2'')$ extracted from the real and imaginary parts of the nano-FTIR spectrum for (a) polystyrene and (b) Kapton.

$Q_V^{sm}/Q_V^{rm} \approx$ constant. While all the details are clearly outlined in Section SI.6 (Supporting Information), the procedure results in

$$\bar{z}_{n>1} \cong \frac{\left(\epsilon_r^{sm}-1\right) Q_V^{sm}}{\left(\epsilon_r^{rm}-1\right) Q_V^{rm}} \approx \frac{\epsilon_r^{sm}-1}{\epsilon_r^{rm}-1} \tag{37}$$

Equation (37) is surprisingly simple, and naturally lends itself to an algebraically straightforward way of explaining why $\bar{z}_{n>1}'$ closely relates to dispersion, and $\bar{z}_{n>1}''$ closely relates to absorption. Furthermore, as we will show, the algebraic inversion of Equation (37), $\bar{z}_{n>1}(\epsilon_r^{sm}, \epsilon_r^{rm}) \rightarrow \epsilon_r^{sm}(\bar{z}_{n>1}, \epsilon_r^{rm})$, provides a simple pathway to transform nano-FTIR data into a model extinction coeffect that closely matches empirical results measured via attenuated total reflection Fourier transform infrared spectroscopy (ATR-FTIR).

Assuming that the reference material being used is nonmetallic, spectrally flat in the IR wavenumber region of interest, and also realizes negligible absorption in the IR wavenumber region of interest, the real (imaginary) part of the reference material's dielectric function remains constant-in-energy, $d\epsilon_r^{rm'}/d\nu \approx 0$ (vanishes, $\epsilon_r^{rm''} \approx 0$). This is the case for the commonly used reference material of crystalline Si (cSi): $\epsilon_r^{rm} = \epsilon_r^{cSi} \cong 11.7 + i\,8.48 * 10^{-4} \approx 11.7$.[44] So, assuming this kind/class of reference material with vanishingly small $\epsilon_r^{rm''}$, the real and imaginary parts of $\bar{z}_{n>1}$ are, approximately,

$$\bar{z}_{n>1}' \approx \frac{\epsilon_r^{sm'}-1}{\epsilon_r^{rm'}-1}, \quad \bar{z}_{n>1}'' \approx \frac{\epsilon_r^{sm''}}{\epsilon_r^{rm'}-1} \tag{38}$$

Apparently the real and imaginary parts of $\bar{z}_{n>1}$ directly relate to ϵ_r^{sm}, the sample material's relative complex dielectric permittivity (i.e., dielectric function): $\bar{z}_{n>1}' \propto \epsilon_r^{sm'} - 1$ and $\bar{z}_{n>1}'' \propto \epsilon_r^{sm''}$. Because the real part of the dielectric function is closely related to dispersion via the refractive index, n,[39,45] Equation (38) qualitatively explains why the real part of $\bar{z}_{n>1}$ has a similar line shape and why it is common to report the real part of $\bar{z}_{n>1}$ as relating to dispersion. Similarly, because the imaginary part of the dielectric function is closely related to absorption via the extinction coefficient, κ,[39,45] Equation (38) qualitatively explains why the imaginary part of $\bar{z}_{n>1}$ has a similar line shape and why it is common to report the imaginary part of $\bar{z}_{n>1}$ as relating to absorption. These relationships are easily observed in Figure 5e,f, and become even more acute in the weak oscillator limit ($n \gg \kappa$), where $n \approx \sqrt{\epsilon_r'}$ and $\kappa \approx \epsilon_r''/(2\sqrt{\epsilon_r'})$;[45,46] as others have also shown by different means.[5c,13a] However, even in the weak oscillator limit, κ still depends on both the real and imaginary parts of the dielectric function, and since far-field transmission-type FTIR absorbance spectra measure κ,[46,47] it stands to reason that $\bar{z}_{n>1}'' \propto \epsilon_r^{sm''}$ alone may not be the best near-field quantity to report as absorption, and compare with other FTIR spectral databases.

The level of connection between $\bar{z}_2''$ and κ for a PS sample is compared in **Figure 8a** by plotting $\bar{z}_2''$ (referenced with respect to cSi) in red alongside ATR-FTIR absorbance data of the same sample in black (spectra are normalized to unity). While the $\bar{z}_2''$ peak at 692 cm^{-1} is red-shifted $\approx$ 2.4 cm^{-1} in comparison to ATR-FTIR absorbance, the similarity is still quite striking and gives credence to the use of $\bar{z}_2''$ as a proxy for absorption, as expected. However, a better agreement can be found with a simple algebraic manipulation of the near-field data. By solving the two equations in Equation (38) for the two unknowns, we can establish functions for real and imaginary parts of the sample's dielectric function in terms of the real and imaginary parts of $\bar{z}_n$: $\epsilon_r^{sm'}(\bar{z}_n', \bar{z}_n'')$ and $\epsilon_r^{sm''}(\bar{z}_n', \bar{z}_n'')$. These can be used to compute an expression for the model extinction coefficient (or refractive index) in terms of $\bar{z}_n'$ and $\bar{z}_n''$; this is because the extinction coefficient is generally a function of the real and imaginary parts of the dielectric function:[45] $\kappa(\epsilon_r^{sm'}, \epsilon_r^{sm''}) \rightarrow \kappa(\bar{z}_n', \bar{z}_n'')$. The normalized result, when considering a cSi reference material as given above, is

$$\bar{\kappa}_{n>1}\left(\bar{z}_2', \bar{z}_2''\right) \cong b\left[\sqrt{114.5\,\bar{z}_n''^2 + \left(1+10.7\,\bar{z}_n'\right)^2} - \left(1+10.7\,\bar{z}_n'\right)\right]^{1/2} \tag{39}$$

where b serves as the constant scaling/normalization parameter; and we note that the 10.7 prefactor to $\bar{z}_n'$ in (38) will be different for different reference materials. As can be seen in Equation (39), $\bar{\kappa}_{n>1}$ depends on both the real and imaginary parts of $\bar{z}_{n>1}$. Inputting the nano-FTIR data for PS (Figure 5e,f) into Equation (39) yields a result that is plotted in blue in Figure 8a. The red-shift relative to the ATR-FTIR data has essentially vanished ($\approx$0.1 cm^{-1}). We note in passing that the higher frequency oscillations in the near-field data are likely from noise, while the comparatively narrower full-width half maximum of the band near $\approx$695 cm^{-1} arises from sampling a nanoscale volume.

The validity and utility of Equation (39) was further tested by conducting ATR-FTIR and nano-FTIR of a Kapton sample. The results are plotted in Figure 8b. As in the PS case, $\bar{\kappa}_2(\bar{z}_2', \bar{z}_2'')$ is a good approximation of the ATR-FTIR absorbance spectrum

which measures κ, and while perhaps more challenging to see on a broader scale, $\bar{\kappa}_2(\bar{z}_2', \bar{z}_2'')$ is again a better estimate of ATR-FTIR peak centers than $\bar{z}_2''$ alone. In particular, the average $\bar{\kappa}_2(\bar{z}_2', \bar{z}_2'')$ peak center is 17% closer to ATR-FTIR peak centers than $\bar{z}_2''$ peak centers (based on an analysis of eight peaks fitted with Lorenz models — see Section SI.7 and Figure S1, Supporting Information). Moreover, a comparison of the $\bar{\kappa}_2(\bar{z}_2', \bar{z}_2'')$ semiquantitative model, Equation (39), with the ratio of reflection coefficients, $\bar{z}_{n>1} \approx \beta^{sm}/\beta^{rm}$, where $\beta^j = (\epsilon_r^j - 1)/(\epsilon_r^j + 1)$, another commonly used first-order approximation,[5c,13a] was also conducted for the Kapton data displayed in Figure 8b. As can be seen in Section SI.7 and Figure S1 (Supporting Information), $\bar{\kappa}_2(\bar{z}_2', \bar{z}_2'')$ matched ATR-FTIR peak centers more closely than $\kappa^{\beta^{sm}/\beta^{rm}}(\bar{z}_2', \bar{z}_2'')$ for all eight peaks in the Kapton data. This increased peak center accuracy of Equation (39), combined with its algebraic simplicity, suggests that it may be a better means of assigning spectral features of nano-FTIR spectra to weak molecular oscillations. As one final note, we stress that this approximation (Equation 39) is most applicable for nano-FTIR in the limit of weak and local molecular oscillations in nonmetal materials (like polymers) referenced to spectrally flat cSi when the second derivative of $\tilde{p}_z^j(\omega)$ is small, and that retrieval of rigorously quantitative values of ϵ_r^{sm} for a general system would require a more thorough handling of Equations (28)–(31) for dipoles in and out of the sample plane, or Equations (32)–(34) for dipoles strictly out of plane and coaxial with the probe.

3. Conclusion

At an increasing rate, scattering-type nano-FTIR is being utilized to conduct nanoscale infrared characterization over an impressive breadth of fields, including meteoritics, chemistry, physics, energy storage, and biology. The broad potential applicability of the method is hard to overstate. In this work, we have provided holistic and quantitative derivations of how nano-FTIR spectra are realized, presenting a self-contained pedagogical work that benefits both beginning and seasoned practitioners. We introduced the technique and rigorously stepped through the detection and signal-processing steps. Along the way, common questions are naturally answered, and connections to past works are highlighted. A new and completely general relation for normalized complex valued nano-FTIR spectra, $\bar{z}_{n>1}(\nu)$, is presented: Equations (28)–(31), which is cast in two forms. In one, $\bar{z}_{n>1}(\nu)$ is written in terms of generalized FTs of local dipole moments oriented both in and out of the sample surface plane. In the other, $\bar{z}_{n>1}(\nu)$ is written in terms of volume integrals of generalized FTs of local electric field components oriented both in and out of the sample surface plane, accompanied by corresponding dielectric functions. This formalism can be used as a springboard for additional rigorous modeling endeavors. Moreover, we developed a new, surprisingly simple yet insightful model, useful in the weak oscillator limit when using a cSi reference. It rationalizes why the real and imaginary parts of complex-valued nano-FTIR spectra relate to dispersion and absorption respectively, Equation (38), and facilitates an approximation to the samples' local extinction coefficient that more closely matches ATR-FTIR data than the imaginary part alone, Equation (39). The extinction coefficient model herein takes as inputs both the real and imaginary parts of normalized complex valued nano-FTIR spectra and can be applied straightforwardly with algebra, without the need for complex computations.

4. Experimental Section

Nano-FTIR: The nano-FTIR spectra displayed in Figure 2 (top-most traces), Figure 5, and Figure 8 were collected with 8 cm^{-1} spectral resolution on a commercial Neaspec system equipped with the broadband nano-FTIR laser option (a DFG mid-IR laser source tunable across five output ranges). As for other hardware options, an MCT infrared detector, a ZnSe beamsplitter, and nano-FTIR AFM probes (Neaspec) were all used for these data sets. Moreover, the collections occurred while the AFM was in a tapping mode with a nominal tapping amplitude of 85 nm. The nano-FTIR/SINS data displayed in Figure 2 (bottom two traces) were collected at Lawerence Berkeley National Laboratory's Advanced Light Source at Beamlines 2.4 and 5.4, as indicated in Figure 2. The data collected at BL 2.4 (red trace, Figure 2) used GeCu detector and a KRS-5 beamsplitter. The data collected at BL 5.4 (dark blue trace, Figure 2) used an MCT detector and KBr beamsplitter. As with the other nano-FTIR measurements, tapping mode was also utilized, and with a nominal tapping mode amplitude of $\approx$ 90 nm. Finally, in all cases, each of the devices were contained within an enclosure purged with Nitrogen.

ATR-FTIR: The ATR-FTIR measurements of PS and Kapton in this work were collected at 4 cm^{-1} resolution and conducted on a Shimadzu IRTracer-100 system with a Ge crystal. The spectroscopy system was contained within a nitrogen-purged enclosure.

Supporting Information

Supporting Information is available from the Wiley Online Library or from the author.

Acknowledgements

The authors kindly acknowledge sources that financially supported this work. Funding to support this work was provided to J.M.L., H.A.B., and R.K. by the Energy & Biosciences Institute through the EBI-Shell program. Funding to support this work was also provided to J.M.L and R.K. from the Assistant Secretary for Energy Efficiency and Renewable Energy, Vehicle Technologies Office, under the Advanced Battery Materials Research (BMR) Program, of the U.S. Department of Energy under Contract No. DE-AC02-05CH11231. Additionally, J.M.L. acknowledges Baylor University for financial support through startup funds. Furthermore, this research also used resources of the Advanced Light Source, a U.S. DOE Office of Science User Facility under contract no. DE-AC02-05CH11231. In particular, Beamlines 2.4 and 5.4 were utilized.

Conflict of Interest

The authors declare no conflict of interest.

Data Availability Statement

The data that support the findings of this study are available from the corresponding author upon reasonable request.

Keywords

infrared nano-spectroscopy, nano-FTIR, nanoscale characterization, SINS, s-SNOM

Received: April 18, 2024
Revised: July 13, 2024
Published online: October 2, 2024

[1] a) K. Nakamoto, *Infrared and Raman Spectra of Inorganic and Coordination Compounds*, John Wiley & Sons, New York **2009**; b) T. Hasegawa, *Quantitative Infrared Spectroscopy for Understanding of a Condensed Matter*, Springer, Berlin, Germany **2017**; c) J. M. Thompson, *Infrared Spectroscopy*, Jenny Stanford Publishing (formerly Pan Stanford Publishing), New York **2018**.

[2] a) H. J. Humecki, *Practical Guide to Infrared Microspectroscopy*, CRC Press, Boca Raton, FL, USA **1995**; b) J. E. Katon, *Micron* **1996**, *27*, 303; c) G. L. Carr, *Rev. Sci. Instrum.* **2001**, *72*, 1613; d) B. C. Smith, *Fundamentals of Fourier Transform Infrared Spectroscopy*, CRC Press, Boca Raton, FL, USA **2011**.

[3] P. M. Ajayan, *Nature* **2019**, *575*, 49.

[4] a) N. Ocelic, A. Huber, R. Hillenbrand, *Appl. Phys. Lett.* **2006**, *89*, 101124; b) X. Chen, D. Hu, R. Mescall, G. You, D. N. Basov, Q. Dai, M. Liu, *Adv. Mater.* **2019**, *31*, 1804774.

[5] a) J. M. Stiegler, Y. Abate, A. Cvitkovic, Y. E. Romanyuk, A. J. Huber, S. R. Leone, R. Hillenbrand, *ACS Nano* **2011**, *5*, 6494; b) J. M. Atkin, S. Berweger, A. C. Jones, M. B. Raschke, *Adv. Phys.* **2012**, *61*, 745; c) F. Huth, A. Govyadinov, S. Amarie, W. Nuansing, F. Keilmann, R. Hillenbrand, *Nano Lett.* **2012**, *12*, 3973; d) H. A. Bechtel, E. A. Muller, R. L. Olmon, M. C. Martin, M. B. Raschke, *Proc. Natl. Acad. Sci. USA* **2014**, *111*, 7191; e) A. Centrone, *Annu. Rev. Anal. Chem.* **2015**, *8*, 101; f) F. Huth, PhD Thesis, Universidad Del Pais Vasco, **2015**; g) E. A. Muller, B. Pollard, M. B. Raschke, *J. Phys. Chem. Lett.* **2015**, *6*, 1275; h) O. Khatib, H. A. Bechtel, M. C. Martin, M. B. Raschke, G. L. Carr, *ACS Photonics* **2018**, *5*, 2773; i) H. A. Bechtel, S. C. Johnson, O. Khatib, E. A. Muller, M. B. Raschke, *Surf. Sci. Rep.* **2020**, *75*, 100493.

[6] A. F. Moslein, M. Gutierrez, B. Cohen, J. C. Tan, *Nano Lett.* **2020**, *20*, 7446.

[7] Y. H. Lu, J. M. Larson, A. Baskin, X. Zhao, P. D. Ashby, D. Prendergast, H. A. Bechtel, R. Kostecki, M. Salmeron, *Nano Lett.* **2019**, *19*, 5388.

[8] a) C. Y. Wu, W. J. Wolf, Y. Levartovsky, H. A. Bechtel, M. C. Martin, F. D. Toste, E. Gross, *Nature* **2017**, *541*, 511; b) G. X. Ni, S. Chen, S. S. Sunku, A. Sternbach, A. S. McLeod, L. Xiong, M. M. Fogler, G. Chen, D. N. Basov, *ACS Photonics* **2020**, *7*, 576.

[9] Z. Yao, X. Chen, L. Wehmeier, S. Xu, Y. Shao, Z. Zeng, F. Liu, A. S. McLeod, S. N. Gilbert Corder, M. Tsuneto, W. Shi, Z. Wang, W. Zheng, H. A. Bechtel, G. L. Carr, M. C. Martin, A. Zettl, D. N. Basov, X. Chen, L. M. Eng, S. C. Kehr, M. Liu, *Nat. Commun.* **2021**, *12*, 2649.

[10] a) S. Dai, Z. Fei, Q. Ma, A. S. Rodin, M. Wagner, A. S. McLeod, M. K. Liu, W. Gannett, W. Regan, K. Watanabe, T. Taniguchi, M. Thiemens, G. Dominguez, A. H. Castro Neto, A. Zettl, F. Keilmann, P. Jarillo-Herrero, M. M. Fogler, D. N. Basov, *Science* **2014**, *343*, 1125; b) A. Fali, S. T. White, T. G. Folland, M. He, N. A. Aghamiri, S. Liu, J. H. Edgar, J. D. Caldwell, R. F. Haglund, Y. Abate, *Nano Lett.* **2019**, *19*, 7725.

[11] M. K. Liu, M. Wagner, E. Abreu, S. Kittiwatanakul, A. McLeod, Z. Fei, M. Goldflam, S. Dai, M. M. Fogler, J. Lu, S. A. Wolf, R. D. Averitt, D. N. Basov, *Phys. Rev. Lett.* **2013**, *111*, 096602.

[12] B. Lyu, H. Li, L. Jiang, W. Shan, C. Hu, A. Deng, Z. Ying, L. Wang, Y. Zhang, H. A. Bechtel, M. C. Martin, T. Taniguchi, K. Watanabe, W. Luo, F. Wang, Z. Shi, *Nano Lett.* **2019**, *19*, 1982.

[13] a) A. A. Govyadinov, I. Amenabar, F. Huth, P. S. Carney, R. Hillenbrand, *J. Phys. Chem. Lett.* **2013**, *4*, 1526; b) A. Fali, S. Gamage, M. Howard, T. G. Folland, N. A. Mahadik, T. Tiwald, K. Bolotin, J. D. Caldwell, Y. Abate, *ACS Photonics* **2020**, *8*, 175.

[14] M. Yesiltas, T. D. Glotch, B. Sava, *Sci. Rep.* **2021**, *11*, 11656.

[15] M. Schnell, M. Goikoetxea, I. Amenabar, P. S. Carney, R. Hillenbrand, *ACS Photonics* **2020**, *7*, 2878.

[16] J. Qian, Y. Luan, M. Kim, K.-M. Ho, Y. Shi, C.-Z. Wang, Y. Li, Z. Fei, *Phys. Rev. B* **2021**, *103*, L201407.

[17] a) I. T. Lucas, A. S. McLeod, J. S. Syzdek, D. S. Middlemiss, C. P. Grey, D. N. Basov, R. Kostecki, *Nano Lett.* **2015**, *15*, 100493; b) J. M. Larson, A. Dopilka, R. Kostecki, *Curr. Opin. Electrochem.* **2024**, *47*, 101548.

[18] X. He, J. M. Larson, H. A. Bechtel, R. Kostecki, *Nat. Commun.* **2022**, *13*, 1398.

[19] G. X. Ni, H. Wang, B. Y. Jiang, L. X. Chen, Y. Du, Z. Y. Sun, M. D. Goldflam, A. J. Frenzel, X. M. Xie, M. M. Fogler, D. N. Basov, *Nat. Commun.* **2019**, *10*, 4360.

[20] a) Z. Fei, M. D. Goldflam, J. S. Wu, S. Dai, M. Wagner, A. S. McLeod, M. K. Liu, K. W. Post, S. Zhu, G. C. Janssen, M. M. Fogler, D. N. Basov, *Nano Lett.* **2015**, *15*, 8271; b) G. X. Ni, L. Wang, M. D. Goldflam, M. Wagner, Z. Fei, A. S. McLeod, M. K. Liu, F. Keilmann, B. Özyilmaz, A. H. Castro Neto, J. Hone, M. M. Fogler, D. N. Basov, *Nat. Photonics* **2016**, *10*, 244.

[21] S. Amarie, P. Zaslansky, Y. Kajihara, E. Griesshaber, W. W. Schmahl, F. Keilmann, *Beilstein J. Nanotechnol.* **2012**, *3*, 312.

[22] a) I. Amenabar, S. Poly, W. Nuansing, E. H. Hubrich, A. A. Govyadinov, F. Huth, R. Krutokhvostov, L. Zhang, M. Knez, J. Heberle, A. M. Bittner, R. Hillenbrand, *Nat. Commun.* **2013**, *4*, 2890; b) X. Zhao, D. Li, Y. H. Lu, B. Rad, C. Yan, H. A. Bechtel, P. D. Ashby, M. B. Salmeron, *Proc. Natl. Acad. Sci. USA* **2022**, *119*, 2200019119.

[23] O. Khatib, J. D. Wood, A. S. McLeod, M. D. Goldflam, M. Wagner, G. L. Damhorst, J. C. Koepke, G. P. Doidge, A. Rangarajan, R. Bashir, E. Pop, J. W. Lyding, M. H. Thiemens, F. Keilmann, D. N. Basov, *ACS Nano* **2015**, *9*, 7968.

[24] L. M. Meireles, I. D. Barcelos, G. A. Ferrari, A. N. P. A. A. de, R. O. Freitas, R. G. Lacerda, *Lab Chip* **2019**, *19*, 3678.

[25] K. J. Kaltenecker, T. Golz, E. Bau, F. Keilmann, *Sci. Rep.* **2021**, *11*, 21860.

[26] B. O'Callahan, O. Qafoku, V. Balema, O. A. Negrete, A. Passian, M. H. Engelhard, K. M. Waters, *Langmuir* **2021**, *37*, 12089.

[27] J. Nishida, P. T. S. Chang, J. Y. Ye, P. Sharma, D. M. Wharton, S. C. Johnson, S. E. Shaheen, M. B. Raschke, *Nat. Commun.* **2022**, *13*, 6582.

[28] R. Wilcken, J. Nishida, J. F. Triana, A. John-Herpin, H. Altug, S. Sharma, F. Herrera, M. B. Raschke, *Proc. Natl. Acad. Sci. USA* **2023**, *120*, 2220852120.

[29] a) X. Chen, Z. Yao, Z. Sun, S. G. Stanciu, D. N. Basov, R. Hillenbrand, M. Liu, *Opt. Express* **2022**, *30*, 11228; b) X. Chen, Z. Yao, S. G. Stanciu, D. N. Basov, R. Hillenbrand, M. Liu, *Opt. Express* **2021**, *29*, 39648.

[30] a) Z. Peng, D. Zhang, S. Ge, J. Meng, *Appl. Sci.* **2023**, *13*, 3400; b) X. Chen, C. F. B. Lo, W. Zheng, H. Hu, Q. Dai, M. Liu, *Appl. Phys. Lett.* **2017**, *111*, 223110; c) F. Mooshammer, M. A. Huber, F. Sandner, M. Plankl, M. Zizlsperger, R. Huber, *ACS Photonics* **2020**, *7*, 344.

[31] a) B. Knoll, F. Keilmann, *Nature* **1999**, *399*, 134; b) J. Renger, S. Grafström, L. M. Eng, R. Hillenbrand, *Phys. Rev. B* **2005**, *71*, 119903; c) R. M. Roth, N. C. Panoiu, M. M. Adams, R. M. Osgood, C. C. Neacsu, M. B. Raschke, *Opt. Express* **2006**, *14*, 2921; d) A. Cvitkovic, N. Ocelic, R. Hillenbrand, *Opt. Express* **2007**, *15*, 8550; e) N. Behr, M. B. Raschke, *J. Phys. Chem. C* **2008**, *112*, 3766; f) J. Aizpurua, T. Taubner, F. J. Garcia de Abajo, M. Brehm, R. Hillenbrand, *Opt. Express* **2008**, *16*, 1529; g) A. A. Govyadinov, G. Y. Panasyuk, J. C. Schotland, *Phys. Rev. Lett.* **2009**, *103*, 213901; h) A. S. McLeod, P. Kelly, M. D. Goldflam, Z. Gainsforth, A. J. Westphal, G. Dominguez, M. H. Thiemens, M. M. Fogler, D. N. Basov, *Phys. Rev. B* **2014**, *90*, 085136; i) P. McArdle, D. J. Lahneman, A. Biswas, F. Keilmann, M. M. Qazilbash, *Phys. Rev. Res.* **2020**, *2*, 023272.

[32] a) I. Rajapaksa, K. Uenal, H. K. Wickramasinghe, *Appl. Phys. Lett.* **2010**, *97*, 073121; b) F. S. Ruggeri, G. Longo, S. Faggiano, E. Lipiec, A. Pastore, G. Dietler, *Nat. Commun.* **2015**, *6*, 7831; c) P. M. Donaldson, C. S. Kelley, M. D. Frogley, J. Filik, K. Wehbe, G. Cinque, *Opt. Express* **2016**, *24*, 1852; d) K. L. A. Chan, I. Lekkas, M. D. Frogley, G. Cinque, A. Altharawi, G. Bello, L. A. Dailey, *Anal. Chem.* **2020**, *92*, 8097; e) D. S. Jakob, A. Centrone, *Anal. Chem.* **2022**, *94*, 15564; f) F. Lu, M. Jin, M. A. Belkin, *Nat. Photonics* **2014**, *8*, 307; g) A. Dazzi, R. Prazeres, E. Glotin, J. M. Ortega, *Opt. Lett.* **2005**, *30*, 2388; h) J. Jahng, E. O. Potma, E. S. Lee, *Proc. Natl. Acad. Sci. USA* **2019**, *116*, 26359; i) D. Nowak, W. Morrison, H. K. Wickramasinghe, J. Jahng, E. Potma, L. Wan, R. Ruiz, T. R. Albrecht, K. Schmidt, J. Frommer, D. P. Sanders, S. Park, *Sci. Adv.* **2016**, *2*, 1501571. j) L. Wang, H. Wang, M. Wagner, Y. Yan, D. S. Jakob, X. G. Xu, *Sci. Adv.* **2017**, *3*, 1700255.

[33] a) J. J. Schwartz, D. S. Jakob, A. Centrone, *Chem. Soc. Rev.* **2022**, *51*, 5248. b) L. Xiao, Z. D. Schultz, *Anal. Chem.* **2018**, *90*, 440; c) A. Dazzi, C. B. Prater, *Chem. Rev.* **2017**, *117*, 5146.

[34] B. Voigtländer, *Scanning Probe Microscopy*, Springer, Berlin, Germany **2016**.

[35] T. J. Parker, *Contemp. Phys.* **1990**, *31*, 335.

[36] D. J. Lahneman, T. J. Huffman, P. Xu, S. L. Wang, T. Grogan, M. M. Qazilbash, *Opt. Express* **2017**, *25*, 20421.

[37] a) J. Belhassen, S. Glass, E. Teblum, G. A. Stanciu, D. E. Tranca, Z. Zalevsky, S. G. Stanciu, A. Karsenty, *Adv. Photonics Nexus* **2023**, *2*, 026002. b) C. Maissen, S. Chen, E. Nikulina, A. Govyadinov, R. Hillenbrand, *ACS Photonics* **2019**, *6*, 1279; c) Z. Zhang, P. Qi, O. Kosavera, M. Deng, C. Gong, L. Lin, W. Liu, https://www.researching.cn/HiringPubPDF/COL-24-0229.pdf.

[38] L. D. Landau, *The Classical Theory of Fields*, Elsevier, Amsterdam **2013**.

[39] J. D. Jackson, *Classical Electrodynamics*, Wiley, New York **1998**.

[40] G. Németh, H. A. Bechtel, F. Borondics, *Opt. Express* **2024**, *32*, 15280.

[41] B. Kusnetz, J. Belhassen, D. E. Tranca, S. G. Stanciu, S.-R. Anton, Z. Zalevsky, G. A. Stanciu, A. Karsenty, *Results Phys.* **2024**, *56*, 107318.

[42] W. K. Panofsky, M. Phillips, *Classical Electricity and Magnetism*, Courier Corporation, Chelmsford, MA, USA **2005**.

[43] N. Ocelic, PhD Thesis, Technische Universität München, **2007**.

[44] E. D. Palik, *Handbook of Optical Constants of Solids*, Academic Press, Cambridge, **1998**.

[45] M. Fox, *Optical Properties of Solids*, Oxford University Press, New York **2010**.

[46] S. Mastel, A. A. Govyadinov, T. V. A. G. de Oliveira, I. Amenabar, R. Hillenbrand, *Appl. Phys. Lett.* **2015**, *106*, 023113.

[47] P. R. Griffiths, J. A. de Haseth, *Science* **2007**, *222*, 297.